Nano Research

ISSN 1998-0124 CN 11-5974/O4
https://doi.org/10.26599/NR.2026.94909059

Research Article

Quaternary medium-entropy nanoalloys with crystalline/amorphous heterointerfaces for highly selective and stable photocatalytic nitrite reduction to ammonia

Chen Yang[1], Xing'an Dong[1](✉), Xian Shi[2], Yuying Wang[3], Huirong Yuan[1], Wendong Zhang[4], Weidong Dai[5], Zhenxiang Cheng[6](✉), Peng Yu[1](✉), Fan Dong[5]

[1] College of Physics and Optoelectronic Engineering, Chongqing Normal University, Chongqing 401331, China

[2] School of Chemistry and Environmental Engineering, Sichuan University of Science & Engineering, Zigong 643000, China

[3] Engineering Research Center for Waste Oil Recovery Technology and Equipment, Ministry of Education, Chongqing Technology and Business University, Chongqing 400067, China

[4] College of Chemistry, Chongqing Normal University, Chongqing 401331, China

[5] Research Center for Carbon-Neutral Environmental & Energy Technology, Institute of Fundamental and Frontier Sciences, University of Electronic Science and Technology of China, Chengdu 611731, China

[6] Institute for Superconducting and Electronic Materials, Faculty of Engineering and Information Sciences, University of Wollongong, North Wollongong, Australia

Nano Res., **Just Accepted Manuscript** • https://doi.org/10.26599/NR.2026.94909059

https://www.sciopen.com/journal/1998-0124 on Jul. 28, 2026

Just Accepted

ABLE OF CONTENTS (TOC)

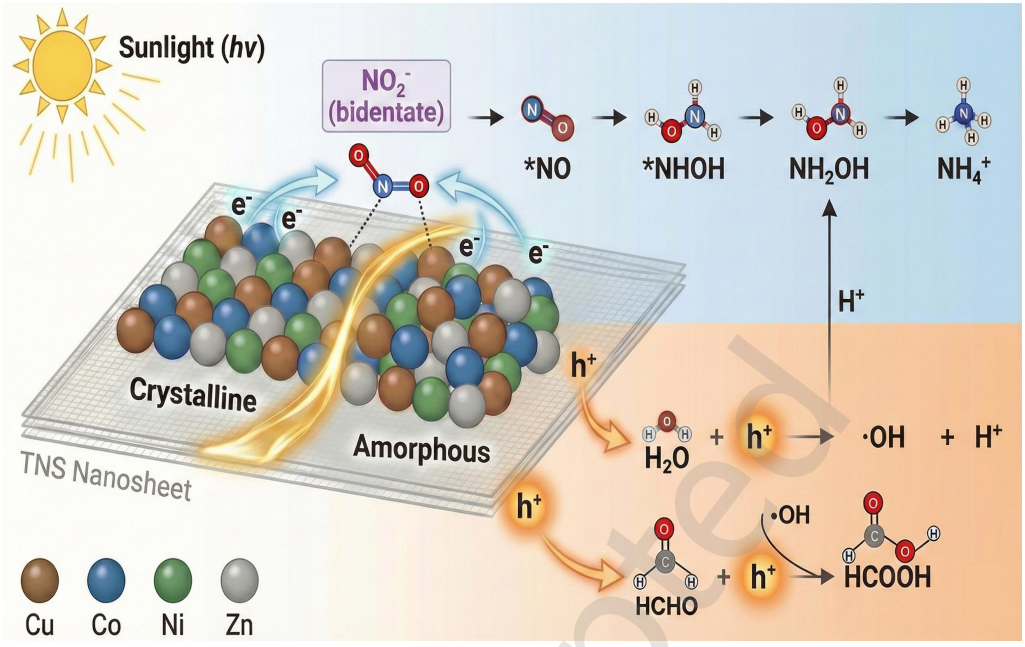

This study develops a quaternary medium-entropy alloy (Cu/Co/Ni/Zn) anchored on TiO_2 nanosheets with engineered crystalline/ amorphous heterointerfaces, which synergistically optimizes nitrite bidentate adsorption and accelerates water dissociation to lower the activation barrier for active hydrogen (*H) generation, while the entropy‐induced sluggish diffusion effect endows the amorphous domains with exceptional stability against photo‐induced recrystallization, collectively achieving a remarkable NH_3 production efficiency of 99.69% with nearly 100% selectivity and superior durability.

Nano Research

Open Access

Research Article

Quaternary medium-entropy nanoalloys with crystalline/amorphous heterointerfaces for highly selective and stable photocatalytic nitrite reduction to ammonia

Chen Yang [1], Xing'an Dong [1] ✉, Xian Shi [2], Yuying Wang [3], Huirong Yuan [1], Wendong Zhang [4], Weidong Dai [5], Zhenxiang Cheng [6] ✉, Peng Yu [1] ✉, and Fan Dong [5]

[1] *College of Physics and Optoelectronic Engineering, Chongqing Normal University, Chongqing 401331, China*
[2] *School of Chemistry and Environmental Engineering, Sichuan University of Science & Engineering, Zigong 643000, China*
[3] *Engineering Research Center for Waste Oil Recovery Technology and Equipment, Ministry of Education, Chongqing Technology and Business University, Chongqing 400067, China*
[4] *College of Chemistry, Chongqing Normal University, Chongqing 401331, China*
[5] *Research Center for Carbon-Neutral Environmental & Energy Technology, Institute of Fundamental and Frontier Sciences, University of Electronic Science and Technology of China, Chengdu 611731, China*
[6] *Institute for Superconducting and Electronic Materials, Faculty of Engineering and Information Sciences, University of Wollongong, North Wollongong, Australia*

Received: 23 May 2026; **Revised:** 2 July 2026; **Accepted:** 28 July 2026

✉Address correspondence to Xing'an Dong, xadong@cqnu.edu.cn; Zhenxiang Cheng, zhenxiang_cheng@uow.edu.au; Peng Yu, pengyu@cqnu.edu.cn

Cite this article: *Nano Research*, 2026, 19, 94909059 https://doi.org/10.26599/NR.2026.94909059

ABSTRACT: Photocatalytic reduction of nitrite (NO_2^-) to ammonia (NH_3) presents a sustainable path for wastewater remediation and nitrogen resource recovery. However, the sluggish seven-proton/six-electron ($7H^+/6e^-$) transfer kinetics and the formidable energy barrier of hydrogen atom transfer (HAT) limit its practical efficiency. Herein, we report a robust photocatalyst comprising quaternary medium entropy alloy (MEA) nanoparticles (Cu, Co, Ni, Zn) anchored on TiO_2 nanosheets (TNS), featuring a tailor-made crystalline/amorphous heterointerfaces. The unique interfacial architecture synergistically optimizes the bidentate adsorption of nitrite and accelerates water dissociation, thereby lowering the activation energy for active hydrogen (*H) generation. Benefiting from the high-entropy-induced "sluggish diffusion" effect, the amorphous domains exhibit exceptional structure stability against photo-induced recrystallization. Consequently, the HH-CCNZ@TNS catalyst achieves a remarkable NH_3 production efficiency of 99.69% with near 100% selectivity, maintaining superior durability over multiple cycles. This work underscores the potential of entropy engineering in coordinating multi-step proton/electron dynamics for advanced energy and environmental catalysis.

KEYWORDS: entropy engineering, crystalline/amorphous heterointerface, photocatalytic reduction, isotope labeling, *in situ* ATR FT-IR

1 Introduction

Ammonia serves as both a high-value-added feedstock for nitrogen fertilizer production and a promising carbon-neutral energy carrier [1]. Currently, NO_2^- is a prevalent pollutant in agricultural and industrial wastewater, posing serious threats to environmental safety and human health [2]. Photocatalytic reduction of nitrite to ammonia (NO_2RR) represents an advanced strategy that integrates pollution control with resource recycling. Driven by solar energy, this approach aims to replace the carbon-intensive Haber-Bosch process [3–6], enabling green ammonia synthesis under mild conditions. However, NO_2RR is a complex multi-electron transfer process involving various potential by-products. Its mechanism can be categorized into two core stages: first, NO_2^- adsorbs onto catalytic active sites and undergoes deoxygenation to form the key intermediate *NO, a step dictated by electronic interactions and NO_x adsorption strength; subsequently, *NO is sequentially protonated to form NH_3, a hydrogenation stage highly dependent on water dissociation and the generation of active hydrogen *H [7, 8].

Nevertheless, NO_2RR involves a daunting six-electron, seven-proton ($7H^+/6e^-$) transfer process. Improper adsorption configurations or excessive adsorption of reactants and intermediates (e.g., *NO_2, NO, *H) can occupy active sites and impede subsequent hydrogenation, while insufficient adsorption may lead to premature desorption and reduced NH_3 selectivity [9]. Therefore, achieving an optimal balance between the adsorption configuration and strength is crucial for directing the reaction pathway toward efficient synthesis. Furthermore, while a sufficient *H supply drives hydrogenation, excessive or

misdirected *H delivery may trigger competitive side reactions [10, 11], such as the hydrogen evolution reaction (HER), thereby reducing NH_3 yield. Consequently, there is an urgent need to develop advanced NO_2RR photocatalysts capable of precisely regulating adsorption configurations and proton dynamics.

Recently, amorphous regions within alloy catalysts have demonstrated significant potential to enhance adsorption and activation due to their abundant coordination-unsaturated sites. However, amorphous structures often suffer from thermodynamic instability and structural reconstruction under external fields [12]. Constructing crystalline/amorphous hetero-interfaces has emerged as an effective strategy to harmonize activity and stability. Recent studies have shown that such interfaces provide [13–15] abundant active sites while ensuring structural stability and electronic conductivity through crystalline regions [12]. This synergistic interaction not only stabilizes the adsorption of NO_2^- but also optimizes the adsorption equilibrium of key intermediates, thereby potentially suppressing competing side reactions that may be induced by excessive *H [16].

Herein, we synthesize a quaternary MEA (consisting of Cu, Co, Ni and Zn) supported on TNS nanosheets with a controllably constructed the crystalline/ amorphous interface. This relatively high configurational entropy (1.27R) suppresses atomic diffusion, effectively maintaining the stability of the hetero-interface during both synthesis and reaction. This structural robustness yields exceptional photocatalytic performance, with NH_3 conversion efficiency consistently exceeding 90% over multiple cycles. Detailed experimental studies reveal that the MEA reduced at 350 °C exhibits unique crystalline/amorphous interfaces, distinct from the fully crystalline (450 °C) or fully amorphous (250 °C) counterparts. Rapid-scan *in situ* FT-IR with isotope labeling ($Na^{15}NO_2$) confirms that this specific interface enables bidentate adsorption of NO_2^-, optimizing the bridging adsorption of the *NO intermediate and facilitating the rapid $NO_2^- \rightarrow NO \rightarrow NH_3$ conversion [17]. Furthermore, D_2O isotope experiments verified that water servers as the proton source. The unique interface architecture enhances water dissociation and boosts HAT efficiency while remaining stable after prolonged photoreaction [18–22]. This work offers a new paradigm for designing hetero-interface structures to regulate the selectivity of complex multistep catalytic reactions.

2. Experimental Section

2.1 Materials:

Copper nitrate hexahydrate ($Cu(NO_3)_2$, Macklin) cobalt nitrate hexahydrate ($Co(NO_3)_2{\cdot}6H_2O$, Macklin), nickel nitrate hexahydrate ($Ni(NO_3)_2{\cdot}6H_2O$, Keshi), zinc nitrate hexahydrate ($Zn(NO_3)_2{\cdot}6H_2O$, Keshi), NaOH (96%, Aladdin), tetrabutyl titanate (98%, Sinopharm Chemical Reagent Co., Ltd), Hydrofluoric acid(HF, 40 wt%, Keshi), potassium nitrite (KNO_2), sodium nitrite ($Na^{15}NO_2$), D_2O (99.9%, Aladdin), Millipore water is used in all experiments.

2.2 Methods

medium-entropy hydrotalcite precursor, which was then anchored onto the surface of anatase-phase TiO_2 via an in-situ regulation strategy, yielding the composite denoted as

2.2.1 Synthesis of TNS

TiO_2 nanosheets with exposed {001} facets (denoted as TNS) were synthesized via a modified hydrothermal method adapted from a previously reported protocol. In a typical procedure, 25 mL of tetrabutyl titanate was mixed with 3.0 mL of hydrofluoric acid (40 wt%, serving as a morphology-directing agent) under vigorous stirring to form a homogeneous precursor solution. The resulting mixture was then transferred into a Teflon-lined stainless-steel autoclave and maintained at 200 °C for 24 h. After the hydrothermal reaction, the white precipitate was collected by centrifugation, washed sequentially with deionized water and ethanol to remove residual organics and loosely bound species. To eliminate adsorbed fluoride ions from the surface, the obtained product was redispersed in an aqueous NaOH solution (0.1 M) and stirred for 24 h. The final product was recovered by centrifugation, washed repeatedly with deionized water until the supernatant reached neutral pH, and finally dried at 60 °C in air, yielding the desired TNS samples.

2.2.2 Synthesis of HH-CCNZ@TNS

A series of metal-loaded $Cu_4Co_{1.5}Ni_{1.5}Zn_{1.5}$@TNS composites were prepared via a rapid co-precipitation method. In a typical procedure, 37.5 mg of $Cu(NO_3)_2$, 17.8 mg of $CoCl_2{\cdot}6H_2O$, 22.3 mg of $Zn(NO_3)_2{\cdot}6H_2O$, and 17.8 mg of $NiCl_2{\cdot}6H_2O$ were dissolved in 25 mL of deionized water under continuous stirring for 30 min to obtain a homogeneous metal salt solution. Concurrently, 3 mmol of the as-synthesized TNS were dispersed in 50 mL of deionized water to form a uniform suspension. The metal salt solution was then added dropwise to the TiO_2 suspension under vigorous stirring, and the resulting mixture was further stirred for 30 min under a constant argon (Ar) flow of 100 $mL{\cdot}min^{-1}$. Subsequently, a 1 M NaOH aqueous solution was added dropwise to adjust the pH of the mixture to approximately 10. The Ar flow rate was then reduced to 60 $mL{\cdot}min^{-1}$, and the stirring was continued for an additional 30 min. The resulting precipitate was collected by centrifugation, washed thoroughly with deionized water, transferred to a glass culture dish, and freeze-dried at –60 °C for 20 h to obtain the CuCoNiZn@TNS photocatalyst (denoted as CCNZ@TNS). To further modulate the interfacial structure, the as-prepared CCNZ@TNS was subsequently calcined at 350 °C for 4 h under a mixed gas atmosphere comprising 40% H_2, 10% CO_2, and 50% Ar. This post treatment yielded a medium-entropy composite photocatalyst featuring a crystalline/amorphous hetero-interface, designated as HH-CCNZ@TNS.

3. Results and Discussion

The architectural evolution of metal-loaded TiO_2 photocatalysts has advanced from simple noble metal modification toward a rational design paradigm that emphasizes multi-component synergy, crystal facet engineering, and defect modulation [23]. Building on this multi-dimensional crystal engineering approach, this study integrates four transition metal ions (Cu^{2+}, Co^{2+}, Zn^{2+}, and Ni^{2+}) in precise stoichiometric proportions. A co-precipitation method was initially employed to construct a quaternary
CCNZ@TNS. Subsequent calcination and hydrogen reduction treatments at various temperatures allowed for the controlled synthesis of medium-entropy alloy composites with distinct

degrees of crystallinity. Specifically, calcination at a high temperature of 450°C readily transforms the metal clusters into a fully crystalline alloy interface (designated as UH-CCNZ@TNS). Conversely, a lower temperature of 250°C preserves the disordered amorphous state (designated as LH-CCNZ@TNS). In contrast, a moderate calcination temperature of 350°C facilitates the formation of a unique and stable crystalline/amorphous heterointerface at the TNS-alloy junction (designated as HH-CCNZ@TNS), providing a rich density of interfacial active sites [24, 25].

The microstructure and elemental distributions of the as-synthesized samples were comprehensively characterized, as presented in Figure 1. Scanning electron microscopy (SEM) images (Figure S1a, b) reveal that the TNS support retains its well-defined nanosheet-like morphology, with metal clusters uniformly dispersed on the TNS surface. X-ray diffraction (XRD) analysis further confirms the crystallographic features of the medium-entropy alloy catalysts. The LH-CCNZ sample exhibits no discernible diffraction peaks, consistent with an amorphous or highly disordered structure [26]. In contrast, the UH-CCNZ sample displays three prominent diffraction peaks at 43.297°, 50.434°, and 74.132°, which are indexed to the (012), (110), and (113) crystallographic planes of the quaternary medium-entropy hydrotalcite-like precursor, respectively [27]. The XRD patterns of HH-CCNZ show intermediate features, suggesting its crystallinity resides between the fully crystalline and amorphous states. Following the loading of the quaternary alloy onto the TiO_2 substrate and subsequent thermal treatments, the XRD patterns of the resulting composite materials reveal distinct diffraction features corresponding to the characteristic planes of the anatase phase of TiO_2 (Figure 1a) [23]. Due to the low mass loading and high dispersion of the Cu-Co-Ni-Zn alloy nanoparticles, as well as their relatively small crystal size, characteristic diffraction peaks of the metallic alloy phase are not significantly detected. The negligible differences observed between the XRD patterns of pure TNS and the CCNZ@TNS series indicate that both the introduction of the alloy species and the hydrogen reduction process do not compromise the crystallinity of the TiO_2 support.

Transmission electron microscopy (TEM) image in Figure 1b-d confirm that Cu, Co, Ni and Zn alloy nanoparticles are successfully supported on the TiO_2 nanosheets following hydrogen-calcination-reduction. Detailed inspection in Figure 1c and 1d highlight the uniform distribution of these nanoalloys across the TNS surface. High-resolution TEM (HRTEM) provides deeper insights into the structural evolution: the lattice spacing of 3.48 Å corresponds to the (101) plane of anatase TiO_2, while the spacing of 1.82 Å is indexed to the (200) crystal planes of the quaternary alloy. Crucially, the lattice fringes of the medium-entropy HH-CCNZ@TNS composite appear locally blurred and disordered, indicating the crystalline and amorphous domains are intimately intertwined to form unique heterointerfaces [28]. Fast Fourier transform (FFT) analysis of region 1 (Figure S2a) exhibits discrete diffraction spots, confirming a crystalline nature, whereas Region 2 (Figure S2b) displays diffuse rings, a hallmark of amorphous domains [29]. Furthermore, the overall morphology of the precursor without H_2 reduction (Figure S3a-c) exhibits a typical nanosheet structure. In contrast, post-reduction samples (Figure S3d-f) reveal metal aggregation zones with varying degrees of crystallinity. Inverse Fast Fourier transform (IFFT) line intensity profiles in Figure 1e further corroborate the existence of these crystalline/amorphous interfaces (Figure S4). This heterogeneous architecture is expected to provide favorable condition environment for NO_2^- adsorption. Inductively coupled plasma optical emission spectroscopy (ICP-OES) analysis confirms that the actual molar ratio of copper, cobalt, nickel, and zinc in HH-CCNZ@TNS is 1:0.47:0.47:0.45, which is broadly consistent with the initially designed stoichiometric molar ratio of 4:1.5:1.5:1.5 (Figure 1e). According to the definition from statistical thermodynamics ($\Delta S_{conf} = -R\sum(X_i \cdot lnX_i)$), X_i represents the mole fraction of the metal species), the configurational entropy (ΔS_{conf}) of the quaternary metals in HH-CCNZ@TNS is calculated to be 1.27R, placing it within the medium-entropy range (1R to 1.5R) [24]. Due to the differences in atomic radii among the four elements-Cu, Co, Ni, and Zn—their random occupation of lattice sites leads to severe local lattice distortions. Such distortions cause fluctuations in the crystal potential field, requiring atoms to overcome higher energy barriers during hopping diffusion compared to conventional metals. The atomic diffusion pathways become distorted and obstructed, thereby kinetically suppressing the long-range migration of atoms [30, 31]. Recent studies have confirmed that, despite the complex enthalpy of mixing relationships in quaternary medium-entropy alloys, there exists a tendency for the elements to form specific chemical short-range order (CSRO). This ordered structure restricts the diffusion pathways of vacancies and interstitial atoms, resulting in a significant reduction in atomic mobility. The limitation imposed by this chemical environment on diffusion pathways represents another key source of the retarded diffusion effect. The retarded diffusion effect induced by lattice distortions and CSRO implies that, even under illumination (which may be accompanied by localized thermal effects or electron excitation), atoms within the amorphous regions struggle to acquire sufficient mobility for cooperative rearrangement. This substantially decreases the likelihood of forming critical nuclei and hinders the growth of pre-existing nuclei by consuming the surrounding amorphous matrix [32]. The dual safeguards of "boundary-free" amorphous regions and "retarded diffusion" ensure that the amorphous regions in HH-CCNZ@TNS remain structurally "frozen" even under illumination conditions that might otherwise induce atomic activation. Consequently, this provides a stable and unique active site environment for NO_2^- adsorption and catalysis.

Finally, high-angle annular dark-field (HAADF) imaging and Energy-dispersive X-ray spectroscopy (EDS) elemental mapping demonstrates that the ~5 nm metal nanoparticles are anchored uniformly on the TiO_2 nanosheets (Figure 1f), with all metallic constituents homogeneously distributed throughout the architecture. Collectively, these morpho-

synthesis of this crystalline/amorphous hetero-phase interfaced medium-entropy nanoalloy composite.

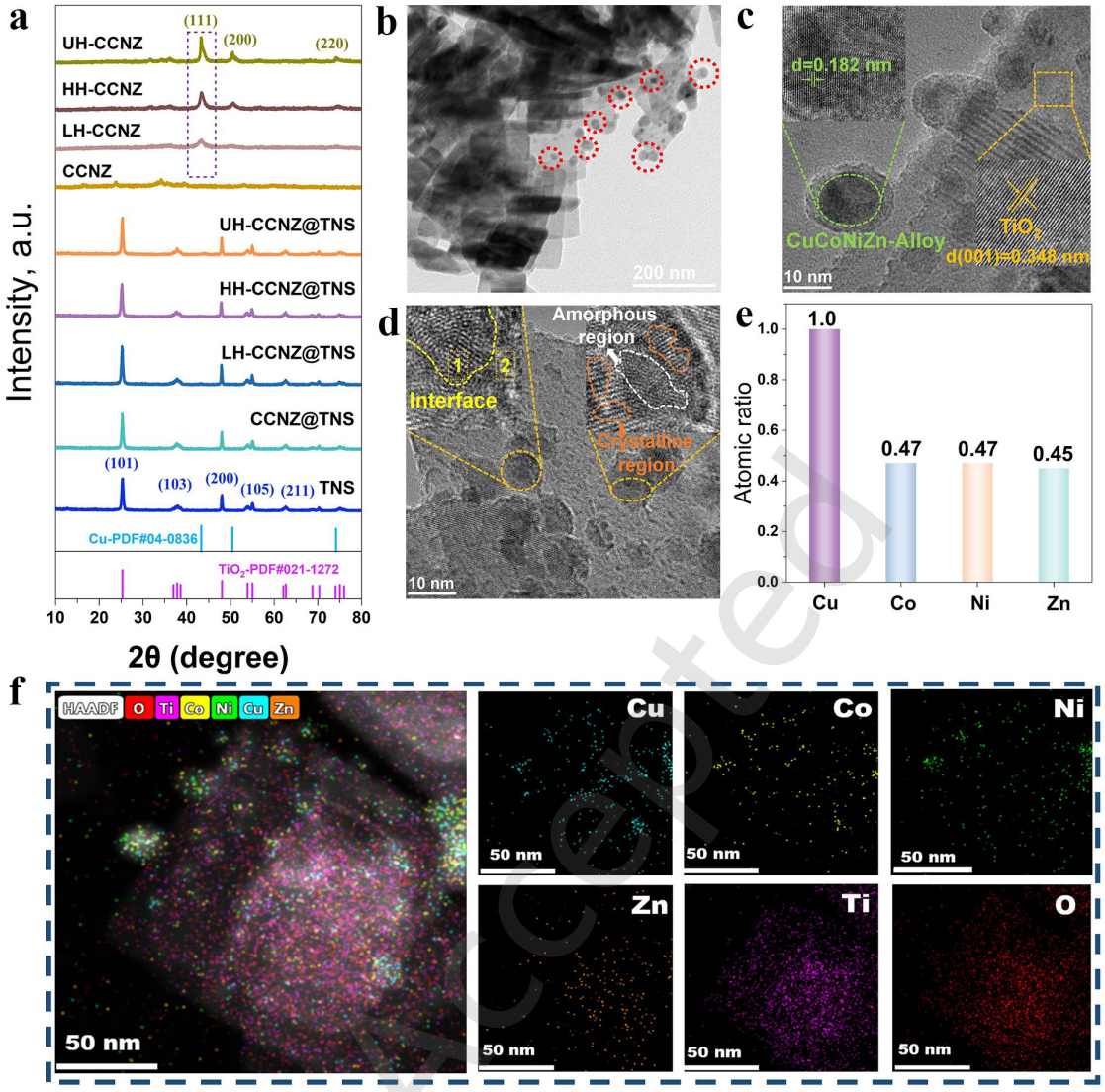

Figure 1. Morphological and structural evolution of HH-CCNZ@TNS catalysts before reaction. (a) XRD patterns. (b) TEM reveals metal nanoclusters supported on TNS, the red-circled area indicates the alloy concentration zone. (c-d) HRTEM, an amorphous/crystalline interface formed in the alloyed region. (e) The atomic ratio of four TM elements. (f) HAADF images and the corresponding EDS elemental maps.

Moreover, we have employed photoelectron spectroscopy to investigate the fine structure of the catalyst material in profound detail. X-ray photoelectron spectroscopy (XPS) was performed to investigate the elemental valence states and interfacial electronic interactions of HH-CCNZ@TNS, LH-CCNZ@TNS, and CCNZ@TNS. The XPS survey spectra (Figure S5) confirm the co-existence of Cu, Co, Ni, Zn, Ti and O elements within the composites. In the Cu 2p spectra (Figure 2a), characteristic Cu^{2+} peaks alongside two satellite peaks are observed in all three samples at specific ratios. Notably, after hydrogen reduction under varying conditions, the Cu 2p binding energy exhibits a distinct negative shift; for instance, the Cu^{2+} binding energy decreases from 932.4 eV in CCNZ@TNS to 931.6 eV in HH-CCNZ@TNS. This downward shift indicates a significant electron transfer from the crystalline TiO_2 domains to the alloy interface. Similarly, the overall binding energies of Co 2p, Ni 2p, and Zn 2p also exhibit systematic negative shifts from CCNZ@TNS to HH-CCNZ@TNS (Figure 2b-2d). This phenomenon is closely associated with the high defect density inherent in the amorphous regions, where the disordered atomic structure provides abundant electron-trapping sites, thereby enhancing electron-accepting capability of the alloy. XPS analysis further reveals that these systematic negative shift in the transition metal binding energies directly confirm the successful construction of an efficient crystalline/amorphous heterointerface within the alloy regions. This architecture establishes a directional electron transfer channel at the interface, synergistically optimizing the material's charge-accepting properties and catalytic utilization efficiency.

To further investigate the band structure of the prepared catalyst, UPS spectra were obtained as shown in Figure 2e. The mid-band maximum energy (E_V) of TiO_2 is lower than that of the Cu Co Ni Zn alloy, indicating a reduced density of states around the Fermi level (E_f) and suggesting enhanced adsorption capacity for intermediate species [33]. The work function of the prepared catalyst was calculated from the secondary electron cutoff energy. As depicted in Figure 2e, the work function (4.21eV) of TiO_2 is lower than that of the Cu Co Ni Zn alloy (4.64 eV). The band contact diagrams for TiO_2 and the Cu Co Ni Zn alloy are shown in Figure 2f. The formation of Cu-Co-Ni-

Zn/TiO_2 heterostructures facilitates electron transfer from TiO_2 to the Cu Co Ni Zn alloy region. Furthermore, the incorporation of Cu Co Ni Zn quaternary metal elements into the TiO_2 catalyst enhances electron interactions and built-in electric field (BIEF), thereby enabling a more efficient electron transfer process.

The direction of electron transfer inferred from UPS is strongly corroborated by XPS analyses. Specifically, the positive shift in the Ti 2p binding energy (Figure S6) indicates a decrease in electron density on the TiO_2 side, whereas the negative shifts observed for the Cu 2p, Co 2p, Ni 2p, and Zn 2p binding energies are consistent with electron accumulation at the Cu-Co-Ni-Zn alloy. Such pronounced interfacial electronic interactions substantially strengthen the BIEF, thereby facilitating efficient charge separation and migration across the heterointerface.

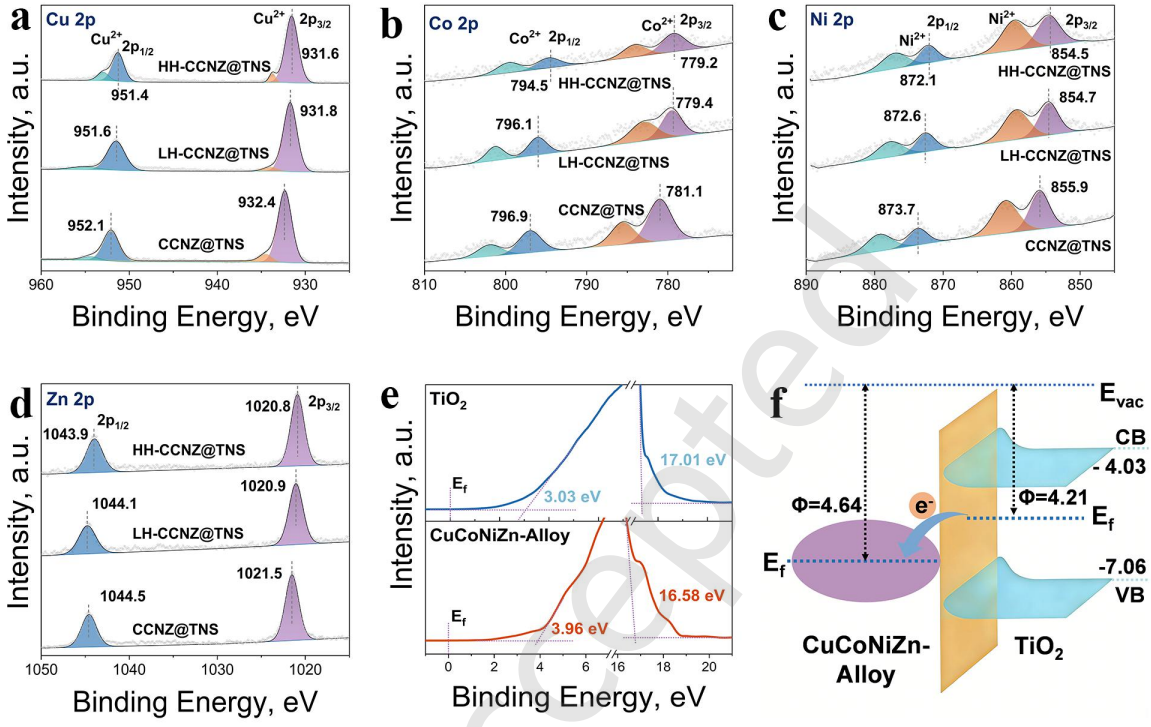

Figure 2. Photoelectron spectroscopy of the catalyst. (a-d) XPS spectra of Ni 2p, Co 2p, Zn 2p and Cu 2p of CCNZ@TNS, LH-CCNZ@TNS, HH-CCNZ@TNS. UPS spectra(e), and energy band diagram of TiO_2, quaternary metal alloy (f).

Building on the advantageous structural features of the synthesized materials, we systematically evaluated their catalytic performance for the NO_2RR. Optimization experiments regarding the Cu: Co: Ni: Zn molar ratios and the degree of hydrogen reduction were conducted. The catalyst screening process commenced with the preparation of a series of quaternary metal ratios on TNS (Figure S8-S12), followed by a comprehensive evaluation of their photocatalytic NO_2^- reduction activities [34]. To further enhance performance, HCHO was employed as a synergistic oxidative reactant to facilitate the half-reaction and assess the reduction activity across various metal configurations [35]. Our results demonstrate that the optimal NO_2RR activity is achieved with Cu: Co: Ni: Zn molar ratio of 4:1.5:1.5:1.5 under a reduction temperature of 350°C (Figure 3a).

Concurrently, the rapid decrease in nitrite concentration (Figure 3b) highlights the superior performance of the medium-entropy alloy composite, which is attributable to its unique crystalline/amorphous heterointerface. The photocatalytic conversion of nitrite approached approximately 100%, corresponding to a nearly quantitative NH_3 selectivity of approximately 100% (Figure 3c), thereby demonstrating sustained and selective reduction.

Notably, the HH-CCNZ@TNS catalyst delivered a remarkable NH_3 production rate of 884 $\mu mol \cdot g^{-1} h^{-1}$ (Figure 3d), surpassing the majority of previously reported photocatalysts [36–41]. Furthermore, the catalyst maintained a consistent NO_2^- removal efficiency of ~100% throughout five consecutive cycling (Figure 3e and 3f), demonstrating excellent long-term stability. In addition, the quantum efficiencies of photocatalytic NO_2-RR of the HH-CCNZ@TNS in the HCHO-free solution as well as HCHO solution were also calculated, which were 0.01% and 0.14%, respectively, demonstrating that the addition of HCHO can substantially enhance the proton transfer efficiency and the utilization of light has been greatly improved. Exceptional performance was also observed during the reduction of high-concentration nitrite (Figure 3g), further attesting to the material robust structural integrity. Remarkably, the MEA-constructed crystalline/amorphous heterointerface remained intact after the photocatalytic reaction (Figure 3h), with the amorphous regions exhibiting no signs of crystallization. In stark contrast, the initially amorphous LH-CCNZ@TNS sample underwent significant crystallization under identical conditions (Figure S13–S14), highlighting the critical role of the crystalline/amorphous heterointerface in stabilizing the amorphous domains against intensive illumination. Moreover, the corresponding EDS elemental mapping spectra acquired after the reaction (Figure 3i) confirm that the composite architecture—metal alloy nanoparticles well dispersed on TiO_2 nanosheets—also remains structurally intact. Collectively, these findings unequivocally demonstrate that the crystalline/amorphous heterointerface not only suppresses

crystallization of the amorphous domains but also guarantees the structural robustness of the catalyst throughout extended photocatalytic operation.

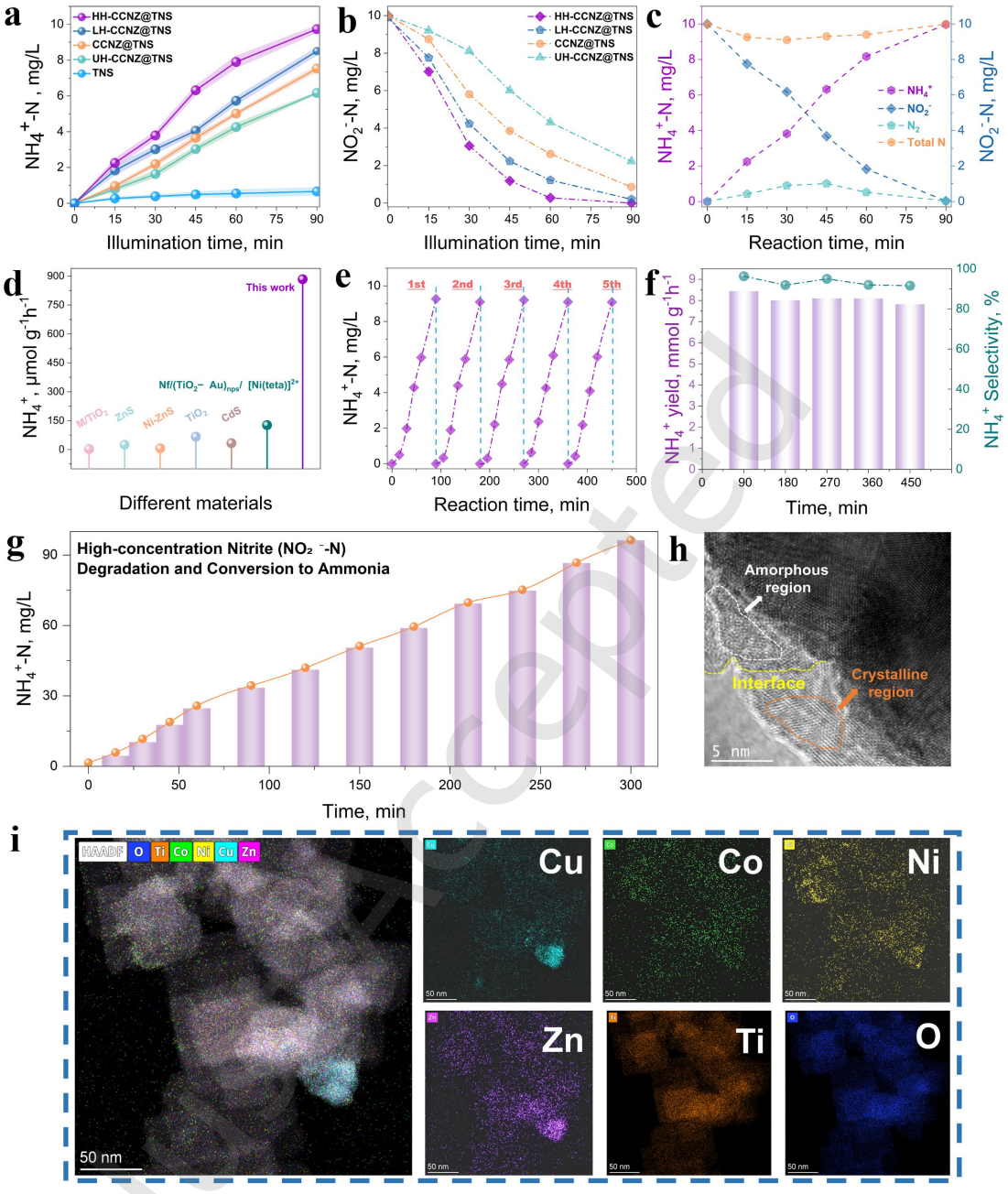

Figure 3. Photocatalytic NO_2^- reduction performance test. Photocatalytic activity of the as-synthesized samples for yield of NH_3 and the removal of NO_2^- (a and b). (c) Selectivity test for the continuous NO_2^- reduction on the HH-CCNZ@TNS photocatalyst. (d) Comparison of the NH_3 synthesis yield of HH-CCNZ@TNS with recently reported photocatalysts. Cycle photocatalytic performance (e and f) of HH-CCNZ@TNS. (g) Long-period photocatalytic performance. (h and i) HAADF images and corresponding EDS elemental mapping spectra of MEA crystalline/amorphous materials after photocatalytic reactions.

To delve into the intrinsic mechanism underlying the enhanced photocatalytic performance of the crystal/ amorphous medium-entropy nanoalloy, we systematically characterized its photoelectrochemical properties and charge carrier dynamics. Ultraviolet-visible diffuse reflectance spectroscopy (UV-vis DRS) reveals that HH-CCNZ@TNS exhibits significant light absorption in the 200–400 nm range, confirming its capability to effectively harvest ultraviolet light to drive the catalytic efficient interfacial electron transport capacity [42, 43]. Steady-state and time-resolved photoluminescence (TRPL) reactions (Figure 4a). Further photoelectrochemical measurements demonstrate that HH-CCNZ@TNS possesses a notably higher photocurrent density compared to control samples (Figure 4b). Additionally, electrochemical impedance spectroscopy (EIS) analysis reveals the minimum charge transfer resistance for HH-CCNZ@TNS (Figure 4c), substantiating the material's superior initial charge separation efficiency and highly

spectroscopy provide more in-depth kinetic evidence regarding carrier behavior: HH-CCNZ@TNS exhibits the weakest

fluorescence emission intensity (Figure 4d),indicating the effective suppression of photogenerated electron-hole pair recombination [44].

Moreover, its average carrier lifetime was calculated to be 32.16 ns, which is significantly longer than that of the benchmark TNS (2.40 ns) (Figure 4e). These results unequivocally indicate that the unique crystalline/ amorphous heterointerface effectively inhibits carrier recombination and provides a prolonged survival time for photogenerated species, thereby substantially increasing their probability of participating in surface catalytic redox reactions. To correlate the aforementioned favorable charge behaviors with specific catalytic reaction pathways, spin-trapping electron spin resonance (ESR) spectroscopy was employed to elucidate the generation of active radicals. Under illumination with the HH-CCNZ@TNS photocatalyst, the characteristic signals of hydroxyl radicals were clearly detected (Figure 4f), which participate in the oxidative half-reaction of formaldehyde [45].

Subsequently, TEMPO was utilized as a probing agent to identify the generation and accumulation of photogenerated electrons (e^-). The intensity of the electron-related signals followed the order of HH-CCNZ@TNS > LH-CCNZ@TNS > CCNZ@TNS > UH-CCNZ@TNS (Figure 4g), exhibiting high consistency with the observed photocatalytic ammonia production performance. This correlation directly demonstrates that the effective yield of photogenerated electrons serves as the kinetic bottleneck determining the NO_2^- reduction efficiency. The unique crystalline/amorphous interface engineered in HH-CCNZ@TNS precisely facilitates the maximization of charge separation and utilization efficiency while simultaneously ensuring long-term structural integrity. These factors synergistically drive the highly selective and efficient synthesis of ammonia.

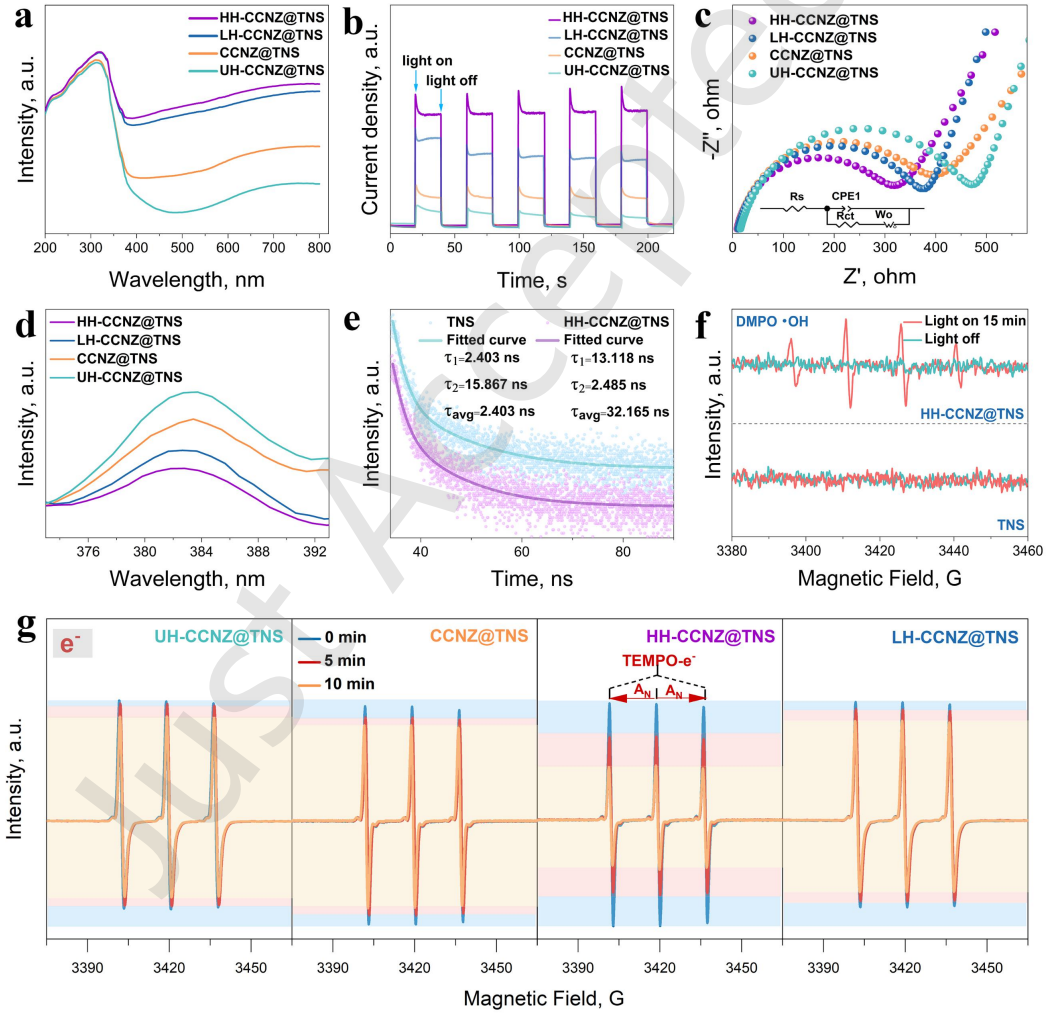

Figure 4. The photoelectric properties of catalyst materials. (a) UV−vis DRS of HH-CCNZ@TNS, LH-CCNZ@ TNS, CCNZ@TNS and UH-CCNZ@TNS. (b) Transient photocurrent response. (c) Nyquist plots. (d) PL spectra. (e) TRPL spectra of TNS and HH-CCNZ@TNS. DMPO spin-trapping ESR spectra for (f) •OH. (g) EPR spectra for LH-CCNZ@TNS, HH-CCNZ@TNS and UH-CCNZ@TNS-e^-.

The photocatalytic reduction of nitrite to ammonia was monitored via rapid-scan *in situ* attenuated total reflection Fourier-transform infrared (ATR FT-IR) spectroscopy. The primary objectives were to obtain in-depth insights into the NO_2^- adsorption and activation process, the formation of reaction intermediates, and the hydrogen atom transfer mechanism, thereby providing robust spectroscopic evidence to elucidate the underlying reaction pathways. Furthermore, the specific NO_2^- adsorption modes and the hydrogen atom transfer

behavior were rigorously investigated via isotope labeling using $Na^{15}NO_2$ and D_2O.

In the spectra obtained using H_2O as the solvent (Figure 5a and 5b), a comparative analysis between $^{14}NO_2^-$ and $^{15}NO_2^-$ (Figure 5d and 5e) reveals two distinct characteristic peaks at 1287 cm^{-1} and 1174 cm^{-1}. These peaks are attributed to the asymmetric and symmetric stretching vibrations of adsorbed NO_2^-, respectively [7, 46]. This appearance of these signals unequivocally indicates the presence of chemically adsorbed nitrite species within the reaction system. Furthermore, a nascent peak at 1404 cm^{-1}, corresponding to the N–H stretching vibration of NH_4^+, is clearly observed during the reaction [22]. This spectroscopic feature directly confirms the successful formation of ammonia and the efficient progression of the photocatalytic nitrite reduction reaction. Based on the rapid-scan *in situ* FT-IR results (Figure 5e), the NO_2RR pathway manifests as follows: adsorbed NO_2^- (1287 cm^{-1}) undergoes deoxygenation followed by stepwise hydrogenation to generate a series of intermediates, including NH_2 (1035 cm^{-1}) and NH_2OH (1206 cm^{-1}), ultimately converting into NH_4^+ (1404 cm^{-1}). The detection of these intermediates suggests that NO_2^- experiences sequential N=O bond cleavage and progressive hydrogenation on the catalyst surface.

Specifically, the bidentate adsorption configuration is identified as a key factor in effectively facilitating N=O bond activation by polarizing the nitrogen-oxygen bonds [22]. Isotopic spectra of KNO_2 and $Na^{15}NO_2$ (Figure 5d) reveal a noticeable red shift in the N=O stretching vibrations; compared to KNO_2, the characteristic peak for $Na^{15}NO_2$ (N=O) shifts toward lower wavenumbers, confirming the nitrogen-involved vibrational nature.

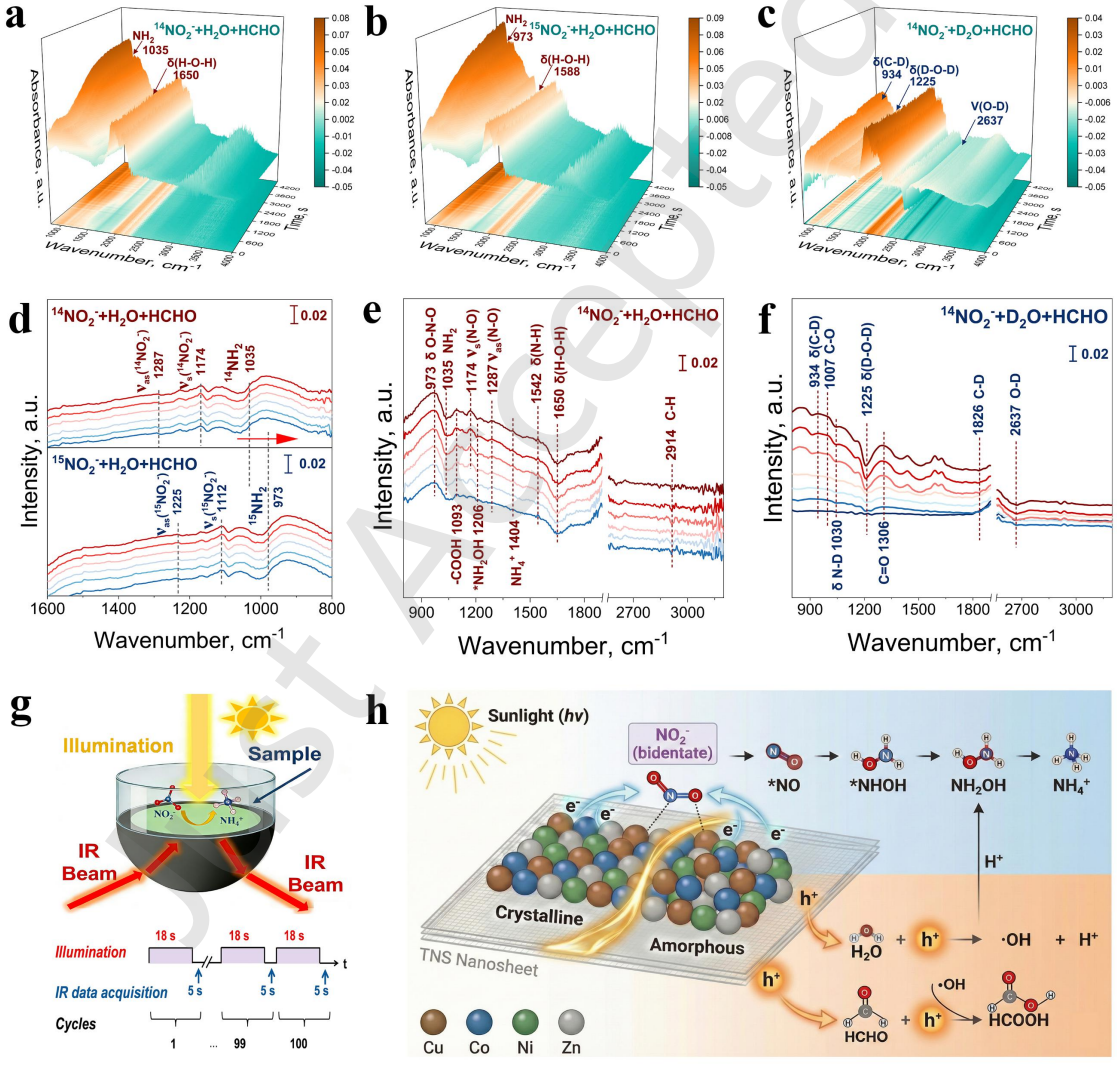

Figure 5. *In situ* FT-IR spectroscopy for probing reaction mechanisms. (a-f) *In situ* FT-IR of KNO_2 and $Na^{15}NO_2$ photoreduction process of HH-CCNZ@TNS tested in the presence of water and deuterium water. *In situ* liquid ATR FT-IR reaction cell: schematic diagram and testing mechanism (g). HH-CCNA@TNS catalyst mechanism for photocatalytic reduction of NO_2^- (h).

Furthermore, the discernible differences in peak shape and width between the isotopes provide additional evidence for the bidentate adsorption mechanism at the interface [22, 47, 48]. Collectively, these spectroscopic features confirm that during the photocatalytic reduction process, NO_2^- is stabilized through bidentate adsorption at the crystalline/amorphous interface, which significantly lowers the energy barrier for the subsequent reduction steps and drives the ammonia production reaction

forward. Notably, in spectra obtained using D_2O as the solvent (Figures 5c, 5f), the characteristic peaks for N–D bending (1030 cm^{-1}), C–D bending (1826 cm^{-1}), and D−O−D bending (1225 cm^{-1}) vibrations all exhibit significant red shift to lower wavenumbers. Their intensities are markedly lower than those of the corresponding N–H (1542 cm^{-1}), C–H (2914 cm^{-1}) [49], and H−O−H bending (1650 cm^{-1}) vibrations observed in the H_2O system. This pronounced isotopic shift highlights the distinct vibrational characteristics of chemical bonds involving deuterium (D) and hydrogen (H) atoms. These observations offer crucial insights into the hydrogen atom transfer mechanism and provide definitive evidence that H_2O serves as the primary proton source for ammonia synthesis. Additionally, the peak intensities of key intermediates in the formaldehyde (HCHO) oxidation process, specifically the C=O stretching (1306 cm^{-1}) and –COOH bending (1093 cm^{-1}) modes, increase progressively over time (Figures 5e, 5f). This trend indicates the gradual oxidation of HCHO under photocatalytic conditions, where the formation and accumulation of these species are characteristic features of the transformation from HCHO to HCOOH. This oxidative half-reaction not only regulates the proton supply by consuming photogenerated holes but also synergistically balances the overall charge transfer for efficient NO_2^- reduction.

ATR FT-IR data acquisition was performed in a periodic light-dark cycle mode (Figure 5g), facilitating the real-time observation of dynamic changes within the reaction system during both the light-excitation and dark-relaxation phases. The core mechanism and the primary highlight of this study reside in the precise regulation and significant enhancement of catalytic sites for the NO_2RR through the rational design of quaternary MEA nanomaterials featuring a crystalline/ amorphous heterogeneous interface. In-situ infrared spectroscopy provides decisive evidence for this proposed mechanism. Firstly, the distinct characteristic peaks of bidentate adsorption (Figure 5h) and their corresponding isotopic shifts directly confirm that NO_2^- is stably anchored at the crystalline/amorphous interface, where the N=O bonds are maintained in an optimal state of polarization and activation. Secondly, the signals of N-D and C-D bonds observed in D_2O isotopic labeling experiments unequivocally reveal that water molecules serve as the ultimate proton source for ammonia production. Simultaneously, the oxidation half-reaction of HCHO regulates this proton supply process by effectively scavenging photogenerated holes. Ultimately, the photogenerated electrons [46], efficiently separated at the interface, and the regulated *H species converge at the active sites. This convergence synergistically drives the continuous and highly selective hydrogenation reduction of NO_2^- to NH_3 [7].

4. Conclusion

The photocatalytic NO_2RR reaction represents a compelling strategy for simultaneous wastewater remediation and restoration of the global nitrogen balance. However, the practical application of this approach has long been constrained by the high energy barrier associated with the HAT process, highlighting the necessity for rational design of advanced catalytic sites. In this study, we successfully constructed a novel composite photocatalyst consisting of semi-crystalline quaternary MEA nanoparticles supported on TNS. The surface of these nanoparticles is enriched with crystalline/amorphous heterointerfaces that facilitate the favorable bidentate adsorption and activation of nitrite, which simultaneously accelerating water dissociation to promote the generation of active hydrogen species. The synergistic medium-entropy effect significantly enhances interface stability and coordinates proton kinetics, resulting in exceptional ammonia production efficiency with near-unity selectivity. Experimental results demonstrate that the MEA reduced at 350°C uniquely retains a stable crystalline/amorphous interface, distinguishing it from structures obtained at other reduction temperatures. This optimized architecture facilitates the rapid conversion of key intermediates ($NO_2^- \rightarrow *NO \rightarrow NH_3$), with water rigorously confirmed as the primary proton source. The unique structure not only enhances water dissociation and HAT efficiency but also remains remarkably stable after prolonged photocatalytic reactions. Collectively, this work provides a new perspective and a robust paradigm for the rational design of heterointerface structures and adsorption configurations, enabling precise regulation of selectivity in complex, multi- step catalytic processes.

Data availability

Supporting Information is available from the author.

Acknowledgements

This work was supported by the National Natural Science Foundation of China (No. 22406014), the Natural Science Foundation of Chongqing (No. CSTB2025NSCQ-GPX0991, CSTB2023NSCQ-LZX0138), the Scientific and Technological Research Program of Chongqing Municipal Education Commission (No. KJQN202400512), the Foundation of Chongqing Normal University (No. 23XLB016) and the Sichuan Provincial Natural Science Foundation (No. 2025NSFTD0003).

Declaration of competing interest

The authors declare no interest conflict. They have no known competing financial interests or personal relationships that could have appeared to influence the work reported in this paper.Author contribution statement

Chen Yang participated in the experiments, conceptualization of the study, and drafting of the initial manuscript. Xian Shi, Yuying Wang, Huirong Yuan, Weidong Dai, Wendong Zhang, and Fan Dong were involved in the reviewing, proofreading, refinement, and language polishing of the manuscript. Xing'an Dong, Zhenxiang Cheng, and Peng Yu contributed to the conceptualization, revision, reviewing, supervision, and final approval of the manuscript. All authors have approved the final version of the manuscript.

References

[1] Ashida, Y.; Arashiba, K.; Nakajima, K.; Nishibayashi, Y. Molybdenum-catalysed ammonia production with samarium diiodide and alcohols or water. *Nature*. **2019**, *568*, 536-540.

[2] Zhu, X.; Fan, X.; Lin, H.; Li, S.; Zhai, Q.; Jiang, Y.; Chen, Y. Highly efficient electroenzymatic cascade reduction reaction for the conversion of nitrite to ammonia. *Adv. Energy Mater.* **2023**, *13*, 2300669.

[3] Li, S.; Ma, P.; Gao, C.; Liu, L.; Wang, X.; Shakouri, M.; Chernikov, R.; Wang, K.; Liu, D.; Ma, R.; Wang, J. Reconstruction-induced NiCu-based catalysts towards paired electrochemical refining. *Energy Environ. Sci.* **2022**, *15*, 3004-3014.

[4] Kyriakou, V.; Garagounis, I.; Vourros, A.; Vasileiou, E.; Stoukides, M.

An electrochemical haber-bosch process. *Joule.* **2020**, *4*, 142-158.
[5] Cheng, X.; Shang, W.; Li, Y.; Hu, J.; Guo, J.; Cao, D.; Zhang, N.; Zhang, S.; Song, S.; Liu, T.; Liu, W.; Shi, Y. Unveiling structural evolution of Fe single atom catalyst in nitrate reduction for enhanced electrocatalytic ammonia synthesis. *Nano Res.* **2024**, *17*, 6826-6832.
[6] Ma, A.; Gui, J.; Huang, Y.; Yu, Y. Electrocatalytic coupling of anodic nitrogen oxidation and cathodic nitrate reduction for ammonia synthesis from air and water. *Nano Res.* **2024**, *17*, 7824-7829.
[7] Mao, J.; Iocozzia, J.; Huang, J.; Meng, K.; Lai, Y.; Lin, Z. Graphene aerogels for efficient energy storage and conversion. *Energy Environ. Sci.* **2018**, *11*, 772-799.
[8] Feng, C.; Wu, H.; Shao, J.; Huo, Q.; Hassan, A.; Yang, H.; Hu, Q.; He, C. Sub‐nanometer‐scale Cu_9S_5 enables efficiently electrochemical nitrate reduction to ammonia. *Adv. Energy Mater.* **2025**, *15*, 2403354.
[9] Li, X.; Shen, P.; Li, X.; Ma, D.; Chu, K. Sub-nm RuO_x clusters on Pd metallene for synergistically enhanced nitrate electroreduction to ammonia. *ACS Nano.* **2023**, *17*, 1081-1090.
[10] Cai, Z.; Zhao, D.; Fan, X.; Zhang, L.; Liang, J.; Li, Z.; Li, J.; Luo, Y.; Zheng, D.; Wang, Y.; Li, T.; Yan, H.; Ying, B.; Sun, S.; Alshehri, A.; Yan, H.; Xu, J.; Kong, Q.; Sun, X. Rational construction of heterostructured Cu_3P@TiO_2 nanoarray for high-efficiency electrochemical nitrite reduction to ammonia. *Small.* **2023**, *19*, 2300620.
[11] Cai, Z.; Ma, C.; Zhao, D.; Fan, X.; Li, R.; Zhang, L.; Li, J.; He, X.; Luo, Y.; Zheng, D.; Wang, Y.; Ying, B.; Sun, S.; Xu, J.; Lu, Q.; Sun, X. Ni doping enabled improvement in electrocatalytic nitrite-to-ammonia conversion over TiO_2 nanoribbon. *Mater. Today Energy.* **2023**, *31*, 101220.
[12] Ma, X.; Yang, T.; He, D.; Gao, X.; Jiang, W.; Li, D.; Sun, Y.; Lin, X.; Xu, J.; Wang, H.; Tai, X.; Lin, Y.; Yao, T.; Zhou, H.; Wu, Y. Carbonate shell regulates CuO surface reconstruction for enhanced CO_2 electroreduction. *Nat. Synth.* **2024**, *4*, 53-66.
[13] Wang, Y.; Hu, J.; Ge, T.; Chen, F.; Lu, Y.; Chen, R.; Zhang, H.; Ye, B.; Wang, S.; Zhang, Y.; Ma, T.; Huang, H. Gradient cationic vacancies enabling inner-to-outer tandem homojunctions for efficient CO_2 photoreduction. *Adv. Mater.* **2023**, *35*, 2302538.
[14] Wu, H.; Zhou, Y.; Han, D.; Wang, Z.; Zhang, S.; Li, J.; Deng, P.; Wu, D.; Tian, X. Self‐healing indium sulfide catalyst for efficient and robust electrocatalytic CO_2 conversion. *Angew. Chem. Int. Ed.* **2025**, *64*, e202505587.
[15] Tan, M.; Huang, B.; Su, L.; Jiao, X.; Feng, F.; Gao, Y.; Huang, Q.; Huang, Z.; Ge, Y. Amorphous nanomaterials: Emerging catalysts for electrochemical carbon dioxide reduction. *Adv. Energy Mater.* **2024**, *14*, 2402424.
[16] Yi, L.; Zhang, Y.; Nie, K.; Li, B.; Yuan, Y.; Liu, Z.; Huang, W. Recent advances in the engineering and electrochemical applications of amorphous-based nanomaterials: A comprehensive review. *Coord. Chem. Rev.* **2024**, *501*, 215569.
[17] Liu, S.; Zhou, F.; Shen, W.; Shi, W.; Shen, X.; Wang, J.; Ge, M.; Wang, M.; Yuan, X.; Yan, C.; Qian, T. Highly efficient ammonia synthesis via electrochemical nitrite reduction using a nitrite reductase-mimicking heterostructured catalyst. *Adv. Funct. Materials.* **2026**, *36*, e14967.
[18] Liao, W.; Wang, J.; Ni, G.; Liu, K.; Liu, C.; Chen, S.; Wang, Q.; Chen, Y.; Luo, T.; Wang, X.; Wang, Y.; Li, W.; Chan, T.-S.; Ma, C.; Li, H.; Liang, Y.; Liu, W.; Fu, J.; Xi, B.; Liu, M. Sustainable conversion of alkaline nitrate to ammonia at activities greater than 2 A cm^{-2}. *Nat. Commun.* **2024**, *15*, 1264.
[19] Shen, H.; Yang, M.; Hao, L.; Wang, J.; Strunk, J.; Sun, Z. Photocatalytic nitrogen reduction to ammonia: Insights into the role of defect engineering in photocatalysts. *Nano Res.* **2022**, *15*, 2773-2809.
[20] Shi, Y.; Chen, L.; Xiong, L.; Wang, X.; Yu, Y.; Yang, M. Synergistic $Cu/Cu_2O/Co_3O_4$ catalyst with crystalline-amorphous interfaces for efficient electrochemical nitrate reduction to ammonia. *Chem. Eng. J.* **2025**, *507*, 160393.
[21] Li, Y.; Wang, C.; Yang, L.; Ge, W.; Shen, J.; Zhu, Y.; Li, C. Enhancement of nitrate-to-ammonia on amorphous CeO_x‐modified Cu via tuning of active hydrogen supply. *Adv. Energy Mater.* **2024**, *14*, 2303863.
[22] Chen, X.; Zhai, S.; Tan, Y.; Su, L.; Zhai, D.; Deng, W.; Wu, H. Enhanced nitrite electroreduction to ammonia via interfacial dual-site adsorption. *J. Energy Chem.* **2024**, *96*, 328-335.
[23] Zhong, W.; Wang, C.; Zhao, H.; Peng, S.; Tian, Z.; Shu, R.; Chen, Y. Synergistic effect of photo-thermal catalytic glycerol reforming hydrogen production over 2D Au/TiO_2 nanoflakes. *Chem. Eng. J.* **2022**, *446*, 137063.
[24] Zhu, L.; Wang, M.; Xiang, S.; Sun, D.; Tang, Y.; Wang, H. A medium-entropy phosphate cathode with multielectron redox reaction for advanced sodium-ion batteries. *Adv. Energy Mater.* **2023**, *13*, 2302046.
[25] Ouyang, X.; Qiao, W.; Yang, Y.; Xi, B.; Yu, Y.; Wu, Y.; Fang, J.; Li, P.; Xiong, S. Intensifying interfacial reverse hydrogen spillover for boosted electrocatalytic nitrate reduction to ammonia. *Angew. Chem. Int. Ed.* **2025**, *64*, e202422585.
[26] Wang, Y.; Li, H.; Zhou, W.; Zhang, X.; Zhang, B.; Yu, Y. Structurally disordered RuO_2 nanosheets with rich oxygen vacancies for enhanced nitrate electroreduction to ammonia. *Angew. Chem. Int. Ed.* **2022**, *61*, e202202604.
[27] Yu, X.; Wang, B.; Wang, C.; Zhuang, C.; Yao, Y.; Li, Z.; Wu, C.; Feng, J.; Zou, Z. 2D high-entropy hydrotalcites. *Small.* **2021**, *17*, 2103412.
[28] Long, Y.; Zhu, X.; Gao, C.; Si, W.; Li, J.; Peng, Y. Modulation of Co spin state at Co_3O_4 crystalline-amorphous interfaces for CO oxidation and N_2O decomposition. *Nat. Commun.* **2025**, *16*, 1048.
[29] Yao, L.; Wu, X.; Geng, Z.; Zhang, Y.; Fang, Y.; Zhu, Q.; Liang, N.; Cai, M.; Sai, H.; Cheng, J.; Li, S.; Wang, Y.; Han, M.; Huang, K.; Feng, S. Oxygen evolution reaction of amorphous/crystalline composites of $NiFe(OH)_x/NiFe_2O_4$. *ACS Nano.* **2025**, *19*, 5851-5859.
[30] Jian, W.; Xie, Z.; Xu, S.; Su, Y.; Yao, X.; Beyerlein, I. Effects of lattice distortion and chemical short-range order on the mechanisms of deformation in medium entropy alloy CoCrNi. *Acta Materialia.* **2020**, *199*, 352-369.
[31] Xie, Z.; Jian, W.; Xu, S.; Beyerlein, I.; Zhang, X.; Wang, Z.; Yao, X. Role of local chemical fluctuations in the shock dynamics of medium entropy alloy CoCrNi. *Acta Materialia.* **2021**, *221*, 117380.
[32] Li, Y.; Du, J.; Shinzato, S.; Ogata, S. Tunable interstitial and vacancy diffusivity by chemical ordering control in CrCoNi medium-entropy alloy. *npj Comput. Mater.* **2024**, *10*, 134.
[33] Zhang, W.; Yang, L.; Li, Z.; Nie, G.; Cao, X.; Fang, Z.; Wang, X.; Ramakrishna, S.; Long, Y.; Jiao, L. Regulating Hydrogen/Oxygen Species Adsorption via Built‐in Electric Field‐Driven Electron Transfer Behavior at the Heterointerface for Efficient Water Splitting. *Angew. Chem. Int. Ed.* **2024**, *63*, e202400888.
[34] Chen, G.; Yuan, Y.; Jiang, H.; Ren, S.; Ding, L.; Ma, L.; Wu, T.; Lu, J.; Wang, H. Electrochemical reduction of nitrate to ammonia via direct eight-electron transfer using a copper–molecular solid catalyst. *Nat. Energy.* **2020**, *5*, 605-613.
[35] Li, J.; Chen, R.; Wang, K.; Yang, Y.; Wang, J.; Yang, W.; Wang, S.; Yang, G.; Dong, F. Combined photoredox catalysis for value-added conversion of contaminants at spatially separated dual active sites. *Research.* **2023**, *6*, 0055.
[36] Ranjit, K.; Viswanathan, B. Photocatalytic reduction of nitrite and nitrate ions to ammonia on M/TiO_2 catalysts. *J. Photochem. Photobiol. A-Chem.* **1997**, *108*, 73-78.
[37] Smith, C.; Torrente-Murciano, L. Guidance for targeted development of ammonia synthesis catalysts from a holistic process approach. *Chem. Catal.* **2021**, *1*, 1163-1172.
[38] Liu, L.; Huang, H.; Chen, Z.; Yu, H.; Wang, K.; Huang, J.; Yu, H.; Zhang, Y. Synergistic polarization engineering on bulk and surface for boosting CO_2 photoreduction. *Angew. Chem. Int. Ed.* **2022**, *61*, e202203519.
[39] Meng, Z.; Yi, J.-H.; Zhang, Y.; Sun, X.; Huang, X.; Shi, M.; Zhang, F.; Yan, J.; Jiang, Q. Intermittent pulsed electrocatalysis adjusting Cu valence states for effective nitrite reduction to ammonia. *Nano Res.* **2025**, *18*, 94907810.
[40] Zhu, Z.; Huang, H.; Liu, L.; Chen, F.; Tian, N.; Zhang, Y.; Yu, H. Chemically bonded α-Fe_2O_3 /Bi_4MO_8Cl dot-on-plate z-scheme junction with strong internal electric field for selective photo-oxidation of aromatic alcohols. *Angew. Chem. Int. Ed.* **2022**, *61*, e202203519.
[41] Liu, B.; Huang, L.; Musho, T.; Chen, C.; Dong, C.; Tang, C.; Yasin, A.; Wang, Y.; Yang, H.; Bright, J.; Zheng, P.; Liu, R.; Wu, N. Oxygen-vacancy-mediated photocatalytic activity of antimony molybdenum oxide toward green ammonia synthesis. *Chem. Catal.* **2025**, *5*, 101337.
[42] Zhang, S.; Xia, Z.; Zou, Y.; Cao, F.; Liu, Y.; Ma, Y.; Qu, Y. Interfacial frustrated lewis pairs of CeO_2 activate CO_2 for selective tandem transformation of olefins and CO_2 into cyclic carbonates. *J. Am. Chem. Soc.* **2019**, *141*, 11353-11357.
[43] Liu, H.; Xie, L.; Suo, R.; Li, W.; Luo, L.; Chen, J.; Lu, C. Efficient Z scheme-type II charge transfer on the interfaces of PAN/ZnO/$CdIn_2S_4$ for the enhanced photocatalytic hydrogen generation. *Int. J. Hydrog. Energy.* **2024**, *63*, 36-47.
[44] Di, J.; Song, P.; Zhu, C.; Chen, C.; Xiong, J.; Duan, M.; Long, R.; Zhou, W.; Xu, M.; Kang, L.; Lin, B.; Liu, D.; Chen, S.; Liu, C.; Li, H.; Zhao, Y.; Li, S.; Yan, Q.; Song, L.; Liu, Z. Strain-engineering of $Bi_{12}O_{17}Br_2$ nanotubes for boosting photocatalytic CO_2 reduction. *ACS Materials Lett.* **2020**, *2*, 1025-1032.
[45] Fang, J.; Zheng, Q.; Lou, Y.; Zhao, K.; Hu, S.; Li, G.; Akdim, O.; Huang, X.; Sun, S. Ampere-level current density ammonia electrochemical synthesis using CuCo nanosheets simulating nitrite reductase bifunctional nature. *Nat. Commun.* **2022**, *13*, 7899.
46] Zhang, C.; Li, J.; Chen, R.; Shen, S.; Wang, J.; Sun, Y.; Dong, F. NH_3 synthesis from N_1 compounds by photocatalytic technology: Promotion

mechanism, reaction pathways, and efficiency evaluation criteria. *ACS Catal.* **2024**, *14*, 15721-15742.

[47] Wu, L.; Feng, J.; Zhang, L.; Jia, S.; Song, X.; Zhu, Q.; Kang, X.; Xing, X.; Sun, X.; Han, B. Boosting Electrocatalytic Nitrate‐to‐Ammonia via Tuning of N‐Intermediate Adsorption on a Zn−Cu Catalyst. *Angew. Chem. Int. Ed.* **2023**, *62*, e202307952.

[48] Mihaylov, M.; Zdravkova, V.; Ivanova, E.; Aleksandrov, H.; Petkov, P.; Vayssilov, G.; Hadjiivanov, K. Infrared spectra of surface nitrates: Revision of the current opinions based on the case study of ceria. *J. Catal.* **2021**, *394*, 245-258.

[49] Shen, S.; Chen, R.; Li, X.; Wang, J.; Yu, S.; Li, J.; Dong, F. Regulating the selectivity of nitrate photoreduction for purification or ammonia production by cooperating oxidative half-reactions. *Environ. Sci. Technol.* **2024**, *58*, 7653-7661.

Electronic Supplementary Material

Quaternary medium-entropy nanoalloys with crystalline/ amorphous heterointerfaces for highly selective and stable photocatalytic nitrite reduction to ammonia

Chen Yang [1], Xing'an Dong [1] ✉, Xian Shi [2], Yuying Wang [3], Huirong Yuan [1], Wendong Zhang [4], Weidong Dai [5], Zhenxiang Cheng [6] ✉, Peng Yu [1] ✉, and Fan Dong [5]

[1] *College of Physics and Optoelectronic Engineering, Chongqing Normal University, Chongqing 401331, China*
[2] *School of Chemistry and Environmental Engineering, Sichuan University of Science & Engineering, Zigong 643000, China*
[3] *Engineering Research Center for Waste Oil Recovery Technology and Equipment, Ministry of Education, Chongqing Technology and Business University, Chongqing 400067, China*
[4] *College of Chemistry, Chongqing Normal University, Chongqing 401331, China*
[5] *Research Center for Carbon-Neutral Environmental & Energy Technology, Institute of Fundamental and Frontier Sciences, University of Electronic Science and Technology of China, Chengdu 611731, China*
[6] *Institute for Superconducting and Electronic Materials, Faculty of Engineering and Information Sciences, University of Wollongong, North Wollongong, Australia*

✉Address correspondence to Xing'an Dong, xadong@cqnu.edu.cn; Zhenxiang Cheng, zhenxiang_cheng@uow.edu.au; Peng Yu, pengyu@cqnu.edu.cn

Supporting information to https://doi.org/10.26599/NR.2026.94909059

Experimental Section

1. Chemicals:

Copper nitrate hexahydrate ($Cu(NO_3)_2$, Macklin) cobalt nitrate hexahydrate ($Co(NO_3)_2{\cdot}6H_2O$, Macklin), nickel nitrate hexahydrate ($Ni(NO_3)_2{\cdot}6H_2O$, Keshi), zinc nitrate hexahydrate ($Zn(NO_3)_2{\cdot}6H_2O$), Keshi), NaOH (96%, Aladdin), tetrabutyl titanate (98%, Sinopharm Chemical Reagent Co., Ltd), Hydrofluoric acid(HF, 40 wt%, Keshi), potassium nitrite (KNO_2), sodium nitrite ($Na^{15}NO_2$), D_2O (99.9%, Aladdin), Millipore water is used in all experiments.

2. Methods

2.1 Synthesis of TNS

TiO_2 nanosheets with exposed {001} facets (denoted as TNS) were synthesized via a modified hydrothermal method adapted from a previously reported protocol [1]. In a typical procedure, 25 mL of tetrabutyl titanate was mixed with 3.0 mL of hydrofluoric acid (40 wt%, serving as a morphology-directing agent) under vigorous stirring to form a homogeneous precursor solution. The resulting mixture was then transferred into a Teflon-lined stainless-steel autoclave and maintained at 200 °C for 24 h. After the hydrothermal reaction, the white precipitate was collected by centrifugation, washed sequentially with deionized water and ethanol to remove residual organics and loosely bound species. To eliminate adsorbed fluoride ions from the surface, the obtained product was redispersed in an aqueous NaOH solution (0.1 M) and stirred for 24 h. The final product was recovered by centrifugation, washed repeatedly with deionized water until the supernatant reached neutral pH, and finally dried at 60 °C in air, yielding the desired TNS samples.

2.2 Synthesis of HH-CCNZ@TNS

A series of metal-loaded $Cu_4Co_{1.5}Ni_{1.5}Zn_{1.5}$@TNS composites are prepared using a rapid co-precipitation method. Specifically, 37.5 mg of $Cu(NO_3)_2$, 17.8 mg of $CoCl_2{\cdot}6H_2O$, 22.3 mg of $Zn(NO_3)_2{\cdot}6H_2O$, and 17.8 mg of $NiCl_2{\cdot}6H_2O$ are dissolved in 25 mL of deionized water under continuous stirring for 30 min to form a homogeneous metal salt solution. Meanwhile, 3 mmol of as-synthesized TNS is dispersed in 50 mL of deionized water to form a suspension. The metal salt solution is then added to the TiO_2 suspension under stirring, and the mixture is stirred for another 30 min under a constant argon (Ar) flow of 100 mL/min. Subsequently, a 1 M NaOH solution is added dropwise to adjust the pH to approximately 10. The Ar flow rate is then reduced to 60 mL/min, and stirring continues for 30 min. The resulting precipitate is collected by centrifugation, washed thoroughly with deionized water, transferred to a glass culture dish, and freeze-dried at –60 °C for 20 h to obtain the CuCoNiZn@TNS photocatalyst. To further modulate the interfacial structure, the as-prepared CCNZ@TNS is calcined under a gas mixture of 40% H_2, 10% CO_2, and 50% Ar at 350 °C for 4 h. This post-treatment results in the formation of a medium-entropy composite photocatalyst with a crystalline/amorphous heterointerface, denoted as HH-CCNZ@TNS

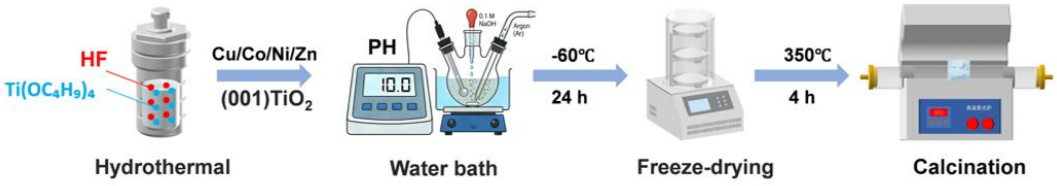

Scheme S1. The synthetic process of HH-CCNZ@TNS composites.

NO_2RR Photoreduction

The photocatalytic ammonia synthesis performance of the synthesized series of medium-entropy composite crystalline/amorphous heterointerface photocatalyst materials HH-CCNZ@TNS is evaluated under xenon (Xe) lamp irradiation, using a 300 W Xe lamp (200–800 nm) as the light source. Additionally, to specifically evaluate the visible-light-driven photocatalytic activity, an optical cutoff filter ($\lambda \geq 420$ nm) was mounted in front of the xenon lamp during the corresponding visible-light photocatalytic tests. This setup ensures that only the visible-light portion of the spectrum (wavelengths greater than 420 nm) can reach the reaction system, while UV light is completely blocked. Forty milligrams of the catalyst are dispersed in 95 mL of an aqueous NO_2^- solution (10 mg/L) with 1 mL of formaldehyde added as a sacrificial agent. The resulting suspension is then transferred to a quartz photocatalytic reactor equipped with a circulating water cooling system to minimize thermal effects. The catalyst suspension is stirred continuously in the dark while being purged with high-purity Ar (99.999%) at a flow rate of 100 mL/min for 30 minutes to remove dissolved oxygen. After this period, the Ar flow rate is adjusted to 60 mL/min, and the reaction is initiated by turning on the 300 W Xe lamp. At specified time intervals, 0.5 mL aliquots of the reaction solution are sampled using a syringe, immediately centrifuged, and filtered through a membrane to remove catalyst particles. The concentrations of NH_4^+, Cl^-, NO_2^-, and NO_3^- formed during the reaction are determined by ion chromatography. For NH_4^+ analysis, a Shimadzu Essentia LC-16i system equipped with a conductivity detector and a Thermo Dionex IonPac™ RFIC™ CS12A column (4×250 mm) is used, with 10 mM methanesulfonic acid as the mobile phase. For the analysis of Cl^-, NO_2^-, and NO_3^-, a Shimadzu Essentia LC-16i system with a conductivity detector and a Shodex IC SI-52 4E column (4×250 mm) is employed, using a 3.6 mM Na_2CO_3 solution as the mobile phase.

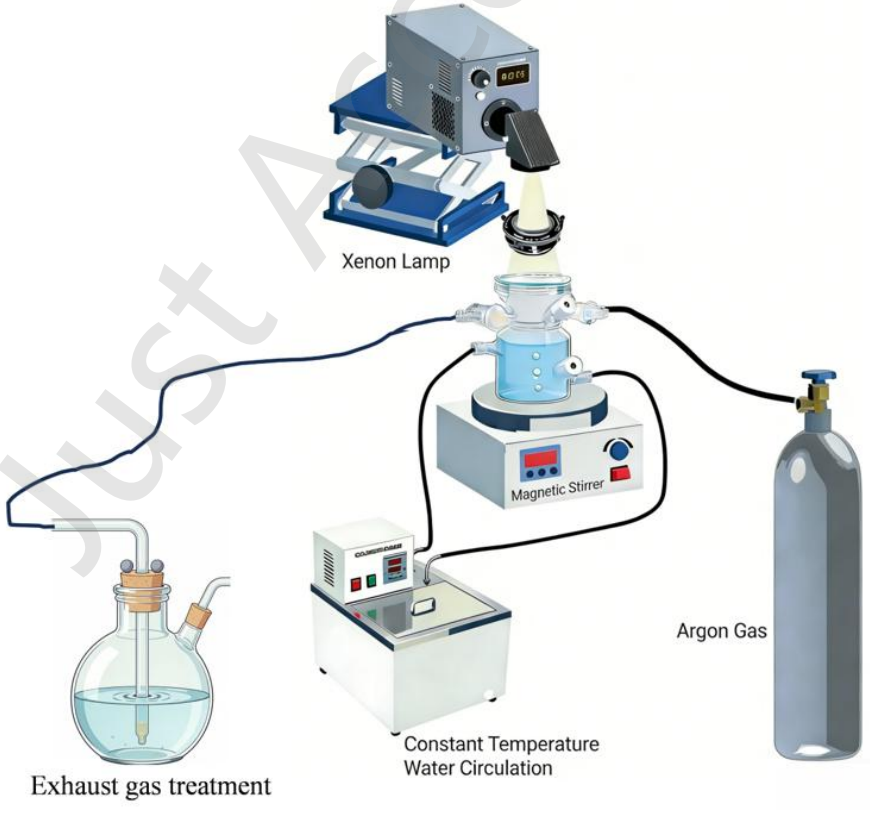

Scheme S2. Photocatalytic testing apparatus for HH-CCNZ@TNS composite materials.

In Situ FT-IR Spectroscopy

In situ FT-IR spectra were collected on a Bruker Vertex 70v FT-IR spectrometer equipped with a narrowband HgCdTe detector and a diamond crystal attenuated total reflectance (ATR) sampling plate (Harrick ConcentratIR 2^{TM}) connected to an evacuation line (~10−7 mbar). The fresh powder sample was dispersed in deionized water and then a drop of the suspension was dropped on the diamond ATR crystal pool. Then the vacuum treatment allows evaporation of the moisture and the sample to be coated on the crystal surface. Subsequently, the sample film was treated in a vacuum to remove the adsorbed water molecules for 30 min.

To detect the NO_2^- adsorption process, in a typical *in situ* FT-IR measurement, a drop of reaction solution was dropped on the sample film. Purity Ar was purged into the ATR crystal pool. When the ATR crystal pool was subsequently purged with high-purity Ar, an adsorption spectrum was detected. In a typical *in situ* FT-IR NO_2^- photocatalytic reduction measurement, a drop of reaction solution was dropped on the sample film. Then, the ATR crystal pool was subsequently purged with high-purity Ar as flow. The ATR crystal pool was then sealed for the subsequent photocatalytic reactions. A 100 mW continuous diode laser (355 nm) was employed as the light source, and a chopped irradiation program with 100 cycles of 18 s irradiation and 5 s dark was performed by periodically intercepting the laser beam with a mechanical shutter (Vincent Associates, model Uniblitz). The shutter was controlled by a BNC pulse/delay generator model 565 and synchronized with the data acquisition in an FT-IR spectrometer. The *in situ* IR spectrum with a spectral resolution of 4 cm^{-1} and scanning velocity of 160 kHz was collected in each 18 s irradiation period of the chopped irradiation program.

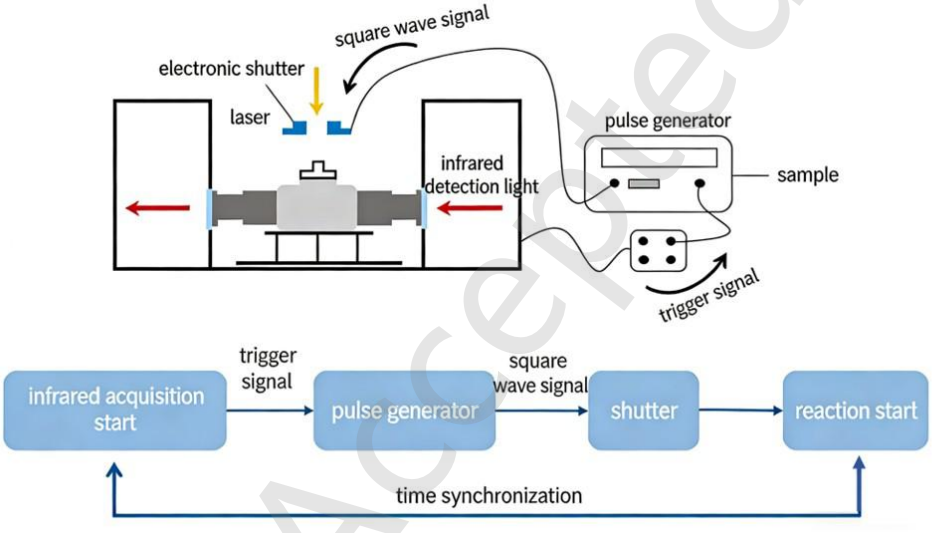

Schematic Diagram S1. Illustrating the mechanism of rapid scanning in situ infrared spectroscopy testing.

Overall, this study confirms that a controlled strategy for fabricating a photocatalyst with an amorphous-crystalline biphasic interface successfully synthesizes a novel medium-entropy composite material, Cu_4 $Co_{1.5}Ni_{1.5}Zn_{1.5}$@TNS (ME-CCNZ@TNS). In this unique medium-entropy photocatalyst, the material's meso-entropy effect enhances the stability of the amorphous-crystalline interface during both synthesis and reaction. In addition, the site regulation at the amorphous/crystalline heterointerface facilitates the bidentate adsorption of nitrite [2–4]. The synergistic effect between this adsorption and the reduction action of the sacrificial agent formaldehyde, combined with the reverse hydrogen spillover mechanism, collectively promotes the kinetic process of reactive hydrogen (*H) in the solution phase. Specifically, these interfaces provide active sites and facilitate *H transfer for the reaction steps. Critically, rational interfacial engineering can markedly amplify this effect, thereby enhancing the performance of photocatalytic nitrite reduction to ammonia and optimizing both ammonia yield and selectivity.

For multi-element alloys, the molar configurational mixing entropy is given by the following formula:

$$\Delta S_{conf} = -R\sum(X_i \cdot lnX_i)$$

The calculated mixing entropy for the Cu_4 $Co_{1.5}Ni_{1.5}Zn_{1.5}$ composition is approximately 1.27 R, which falls precisely within the classic range of medium-entropy materials. This relatively high mixing entropy is one of the key factors contributing to the formation of a stable solid solution phase and potentially superior properties, such as high strength, excellent corrosion resistance, and enhanced catalytic activity.

Photo flux calculation.

The photon flux was calculated and obtained based on the following formulas:

$$\Theta = \frac{N}{S \cdot T}$$

$$N = \frac{P \cdot T \cdot \bar{\lambda}}{h \cdot c}$$

$$P = \bar{E} \cdot S$$

$$\Theta = \frac{\bar{E} \cdot \bar{\lambda}}{h \cdot c}$$

where Θ was the photo flux, N was the incident photon number, S stood for the illumination area of 28.26 cm^{-2}, T referred to the illumination time, h corresponded to the Planck constant, c stood for the speed of light, λ referred to wavelength, $\bar{\lambda}$ referred to an average wavelength (in this work the equivalent $\bar{\lambda}$ was 549.2 nm according to the light source used in this work, provided by the Beijing Merry Change Technology Co., Ltd.), $\bar{E}$ was the average optical power density measured by the optical power meter (Beijing Merry Change Technology Co., Ltd.). Thus, the photon flux Θ could be

$$\Theta = \frac{\bar{E} \cdot \bar{\lambda}}{h \cdot c} = \frac{516.2 \times 549.2 \times 10^{-9}}{6.626 \times 10^{-34} \times 3 \times 10^{8}} = 1.426 \times 10^{21}\ s^{-1} \cdot m^{-2}$$

Quantum efficiency calculation.

The quantum efficiency was defined by the ratio of the effective electrons used for product formation to the total input photon flux. The reduction of NO_2^- molecules to NH_3 molecule requires eight electrons:

$$QE = \frac{\text{effective electrons}}{\text{total photons}} \times 100\% = \frac{6X \cdot N}{\Theta \cdot T \cdot S} \times 100\%$$

Since neither NO_3^- nor N_2 products were detected, where X is the yield from NH_4^+ evolution only, N was Avogadro's number, Θ was the photon flux, T was the irradiation time, and S was the illumination area. The following calculation example was based on the data from the 1 h NO_2^- photoreduction: X =3.88×10^{-6} mol in HCHO free solution and 5.25×10^{-5} mol in HCHO solution, N = 6.022×10^{23} mol^{-1}, T = 3600 s, S = 28.26 cm^2, equivalent Θ = 1.41 × 1017 s^{-1} cm^{-2}. Thus, the quantum efficiency

$$QE\left(NO_2^- RR \text{ without HCHO}\right) = \frac{6X \cdot N}{\Theta \cdot T \cdot S}$$

$$= \frac{6 \times 3.88 \times 10^{-6} \times 6.22 \times 10^{23}}{1.426 \times 10^{21} \times 3600 \times 28.26 \times 10^{-3}} \times 100\% = 0.01\%$$

$$\text{QE}\left(NO_2^- \text{RR with HCHO}\right) = \frac{6\text{X}\cdot\text{N}}{\Theta\cdot\text{T}\cdot\text{S}}$$

$$= \frac{6 \times 5.25 \times 10^{-5} \times 6.22 \times 10^{23}}{1.426 \times 10^{21} \times 3600 \times 28.26 \times 10^{-3}} \times 100\% = 0.14\%$$

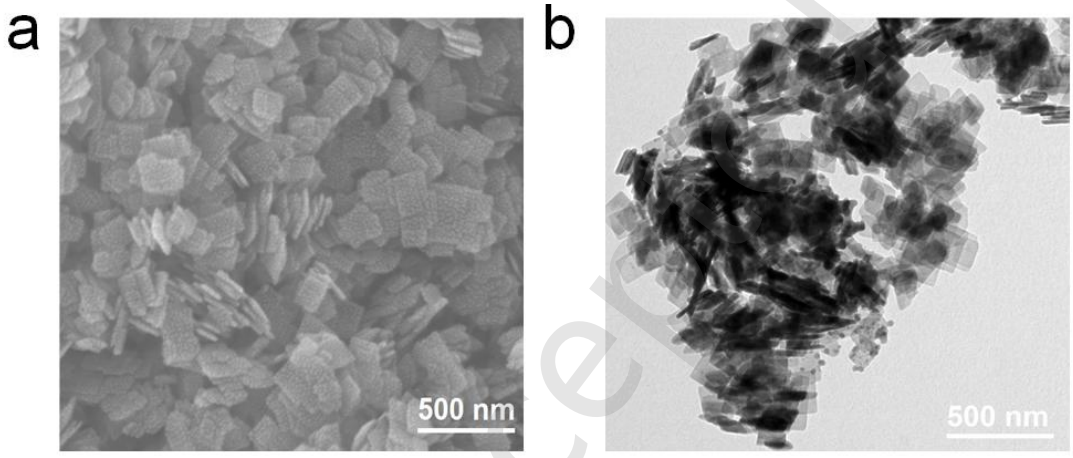

Figure S1. a) The SEM image of titanium dioxide nanosheets. b) SEM image of the composite material formed by loading a quaternary metal alloy onto titanium dioxide.

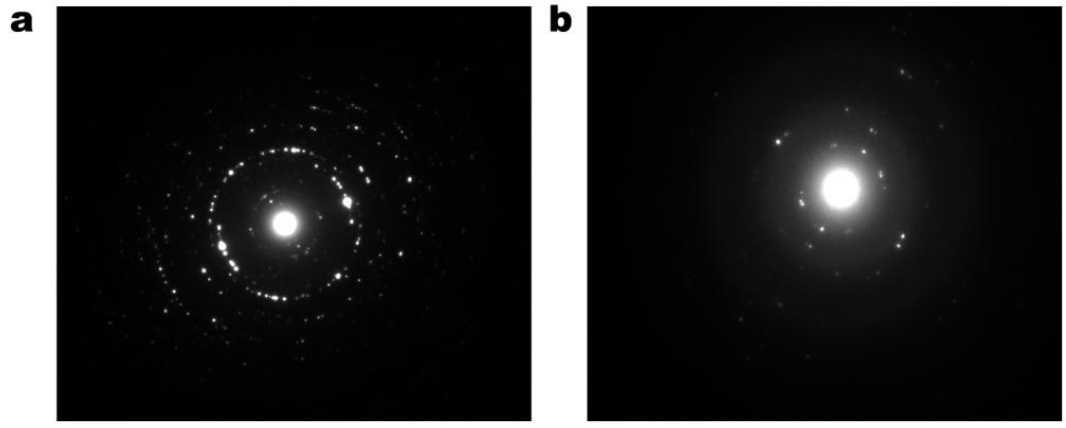

Figure S2. a) Fast Fourier transform (FFT) analysis of region 1 displays discrete diffraction spots in the crystalline area. b) Region 2 indicates diffuse rings characteristic of amorphous domains. Figure a shows the selected electron diffraction pattern of the crystalline region at the alloy interface, obtained from HH-CCNZ@TNS calcined and reduced at 350°C. Figure b displays the selected electron diffraction pattern of the amorphous region at the alloy interface, exhibiting a diffractogram pattern.

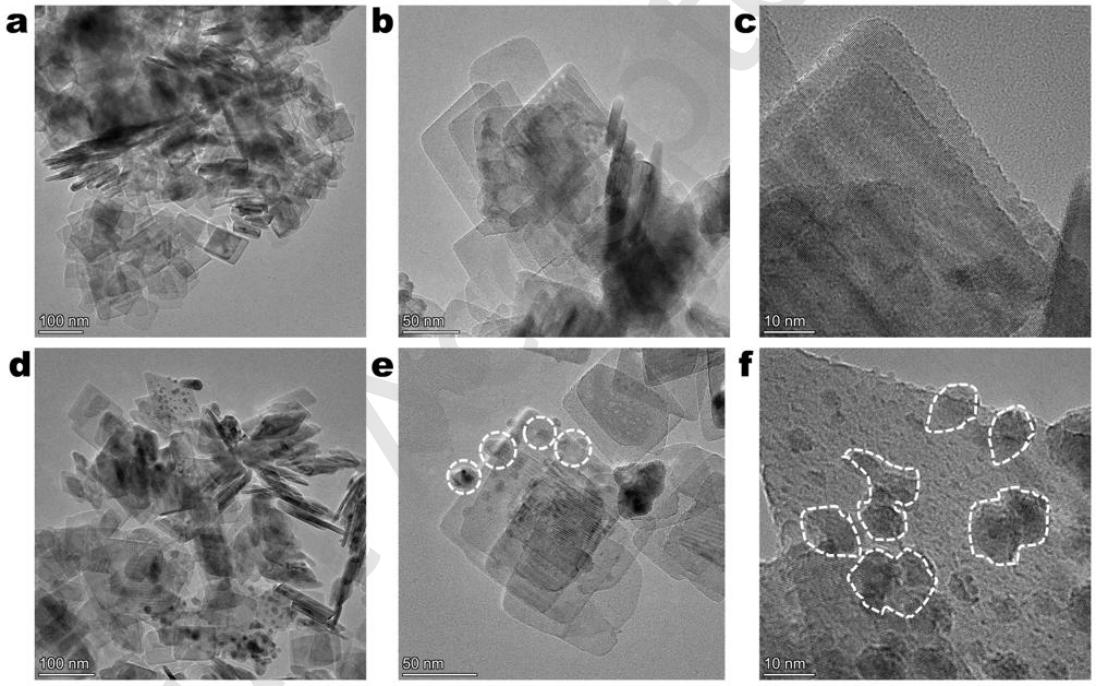

Figure S3. a-c) display transmission electron microscopy (TEM) images of the CCNZ@TNS material. The corresponding images for the HH-CCNZ@TNS material, which was subjected to high-temperature calcination/reduction in a hydrogen atmosphere, are shown in (d-f). The regions encircled in white are attributed to the aggregation of metallic species generated during the reduction process.

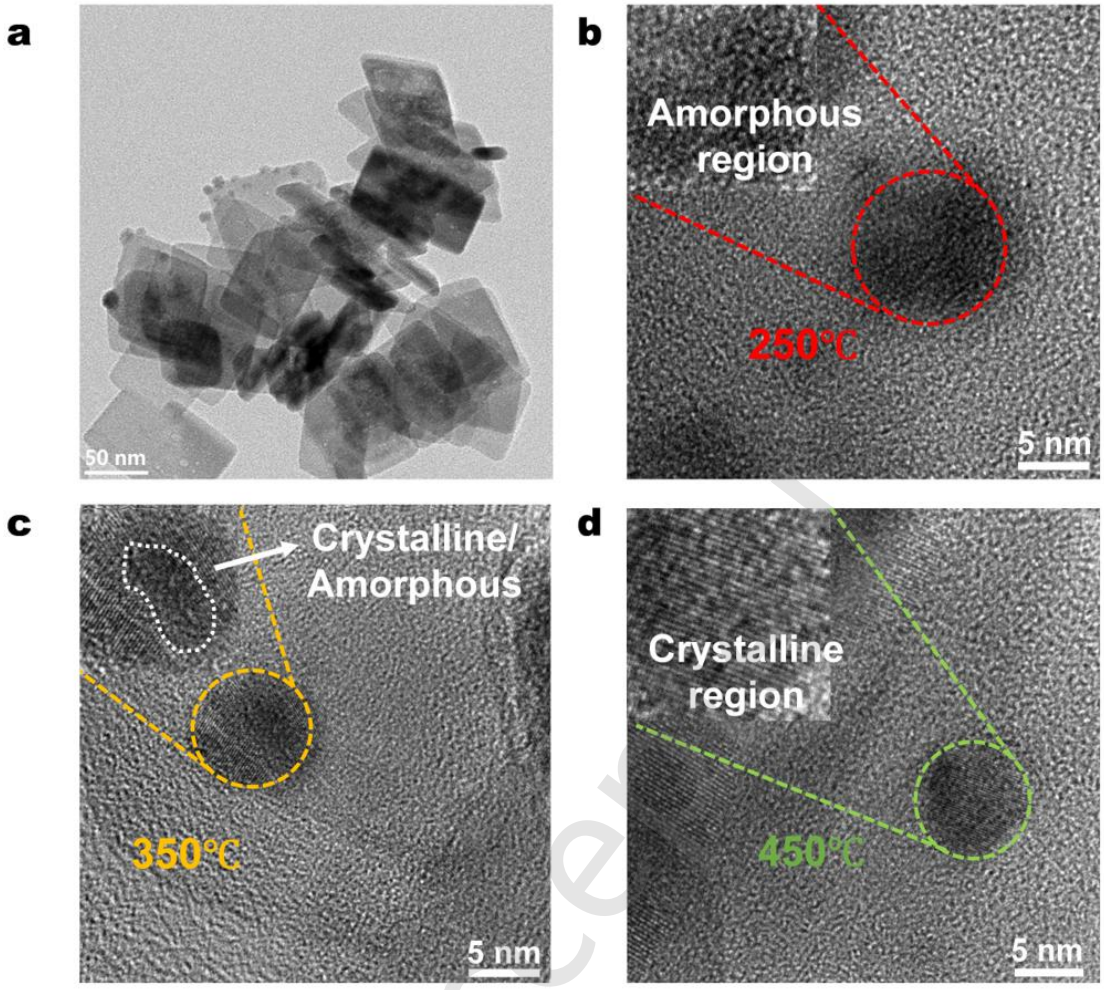

Figure S4. a) TEM images of the sample after the calcination-reduction process. b-d) The intensity distribution profiles extracted from inverse Fast Fourier Transform (IFFT) processing of selected regions in LH-CCNZ@TNS, HH-CCNZ@TNS, and UH-CCNZ@TNS consistently demonstrate interfacial structural features that provide conclusive evidence for the presence of well-defined crystalline/amorphous interfaces.

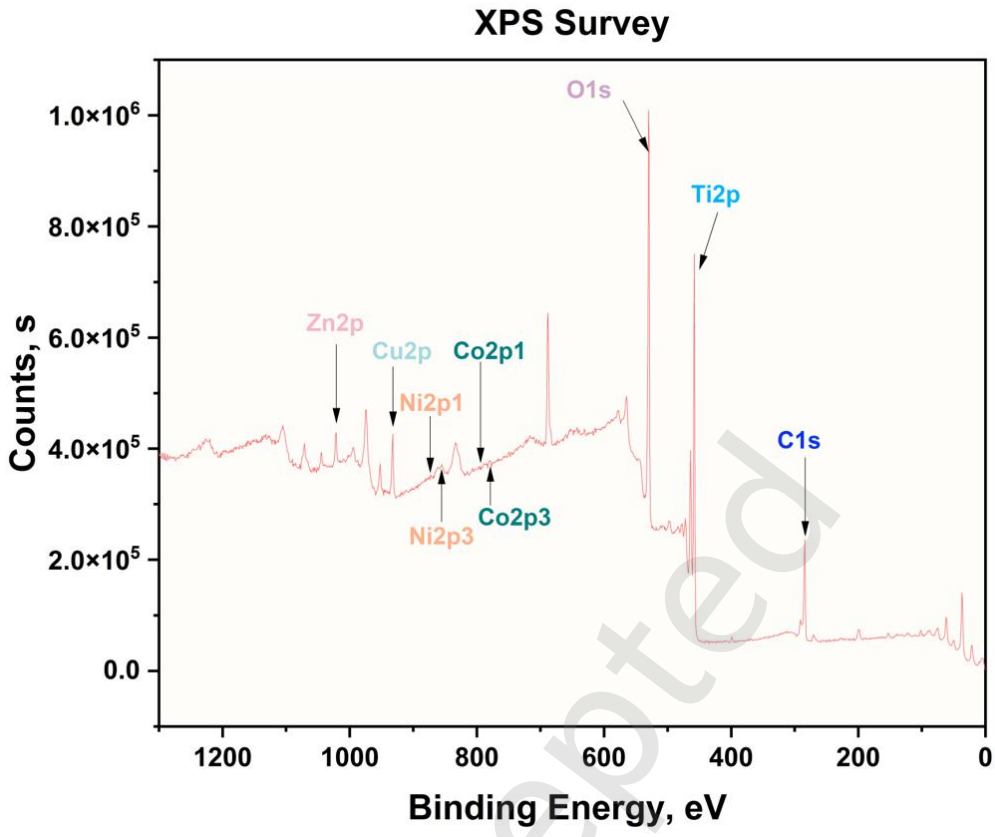

Figure S5. The XPS survey spectrum demonstrates the co-existence of seven elements (Cu, Co, Ni, Zn, Ti, O, and C) in the material system, with distinct photoelectron peaks observed for each elemental constituent.

The Ti 2p spectra (Figure S6) reveal characteristic peaks at approximately 458.5 eV for HH-CCNZ@TNS, CCNZ@TNS, and TNS, corresponding to Ti^{4+} species. Notably, compared to the control sample without hydrogen reduction treatment (TNS), the hydrogen-reduced photocatalyst composites (HH-CCNZ@TNS and CCNZ@TNS) exhibit a positive binding energy shift in their Ti 2p spectra. This systematic shift indicates that the extent of hydrogen calcination-reduction significantly enhances electronic interactions at the interface.

Furthermore, complementary O 1s spectral analysis (Figure S7) demonstrates three characteristic peaks at binding energies of 532.6, 531.5, and 530.1 eV [5], corresponding to adsorbed oxygen species (O_{ads}), metal–oxygen bonds (M–O), and lattice oxygen ($O_{(latt)}$), respectively. Quantitative analysis of oxygen speciation reveals that controlled hydrogen calcination-reduction significantly increases the concentration of M–O bonds while reducing the content of adsorbed oxygen. This transformation is likely associated with lattice distortions induced by the heterophase interface between amorphous and crystalline domains, which promotes the formation of metal–oxygen bonds. The M–O bonds establish stable electron transfer pathways between metal active sites and the TiO_2 support. Under illumination, photogenerated electrons from TiO_2 can rapidly migrate to metal sites via the M–O bonds, effectively suppressing electron–hole recombination. Moreover, the formation of metal–oxygen bonds modifies the local electronic structure, creating an interfacial built-in electric field that facilitates directional electron transfer and accelerates electron accumulation at reactive sites. Within the M–O framework, metal sites (e.g., Cu–O, Co–O) preferentially adsorb NO_2^- ions through coordination interactions, where oxygen atoms stabilize NO_2^- while metal sites elongate the N–O bonds, thereby promoting bond cleavage. This synergistic mechanism further enhances the efficiency of photocatalytic nitrite reduction to ammonia.

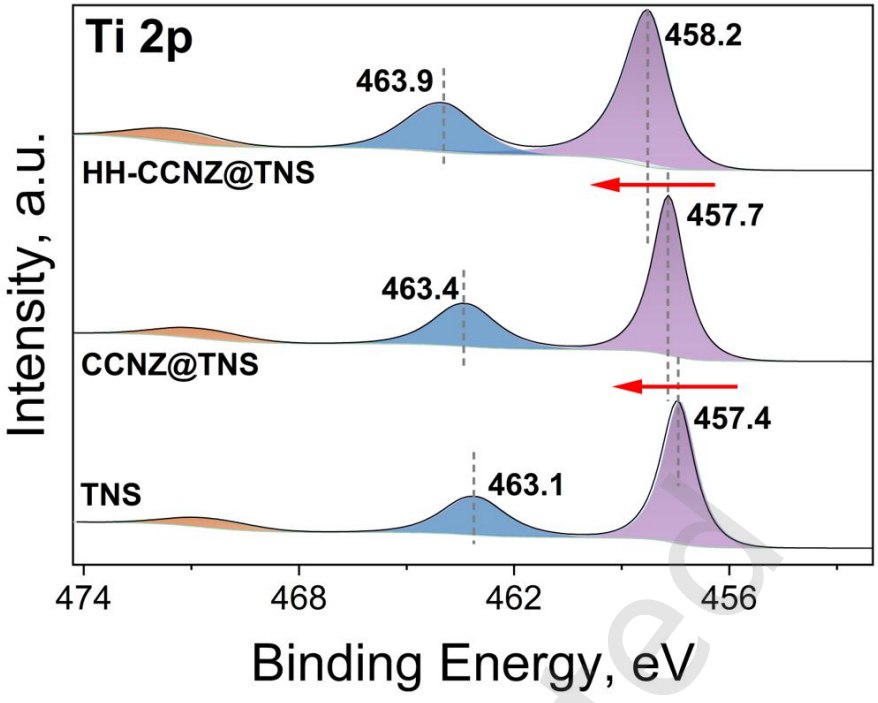

Figure S6. Ti 2p XPS spectrum, the hydrogen-reduced photocatalyst composites (HH-CCNZ@TNS, CCNZ@TNS and TNS) exhibit positive binding energy shifts in their Ti 2p spectra.

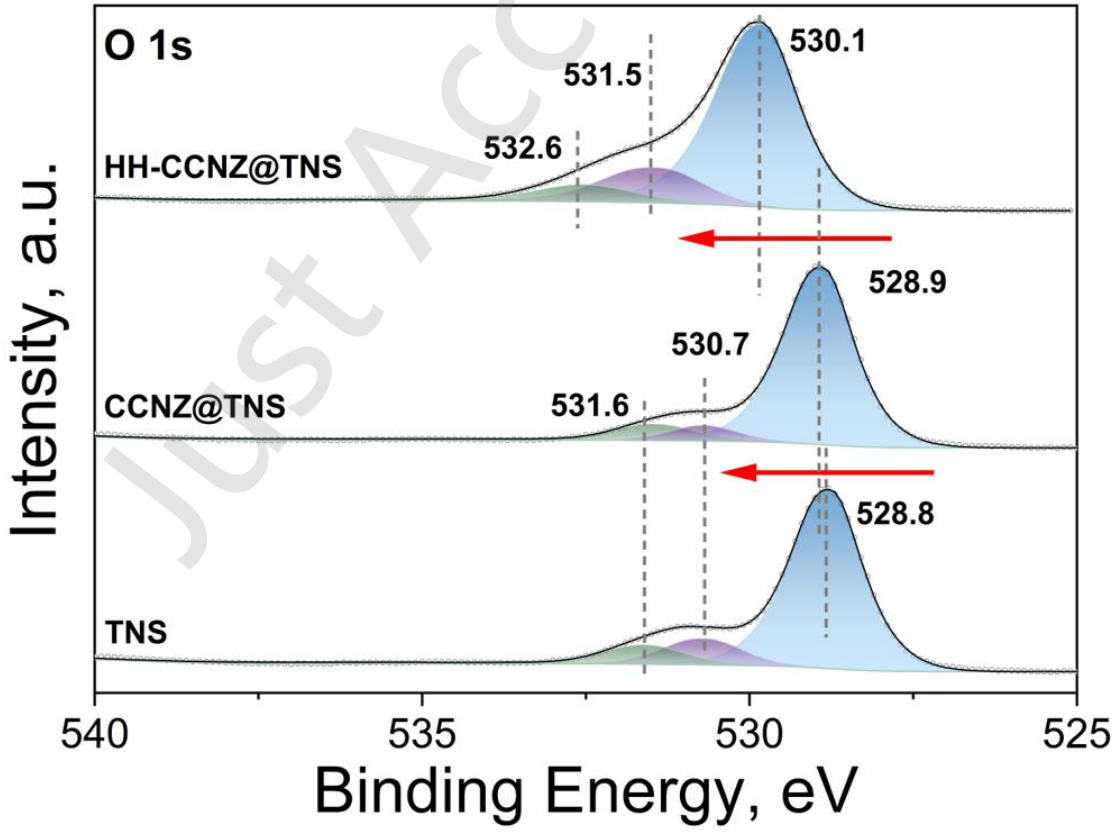

Figure S7. O 1s XPS spectrum, Quantitative analysis of oxygen speciation indicates that controlled hydrogen calcination reduction significantly enhances the M-O bond concentration while diminishing adsorbed oxygen content.

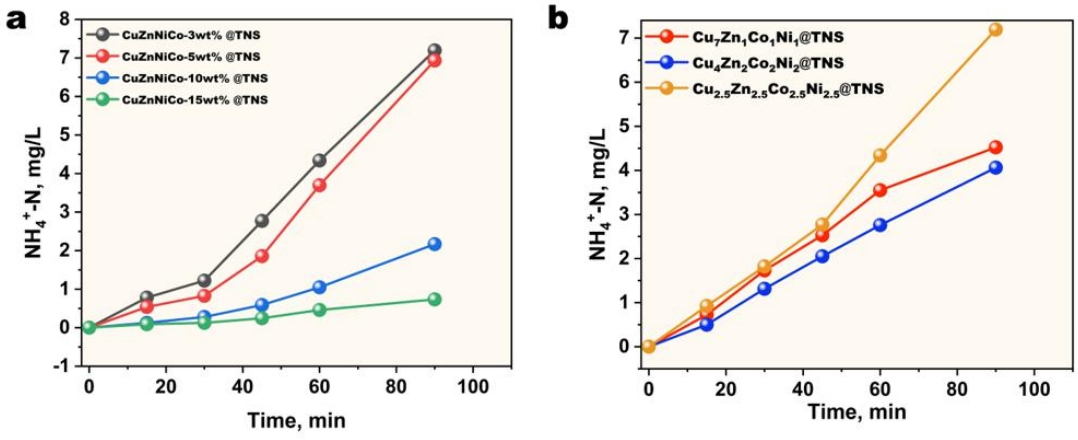

Figure S8. a, b) Investigating which metal (Cu, Co, Ni, or Zn) in a quaternary metal/ TiO_2 photocatalyst acts as the primary active site for enhancing the efficiency of nitrite nitrogen reduction to ammonia, and optimizing the respective loading ratios.

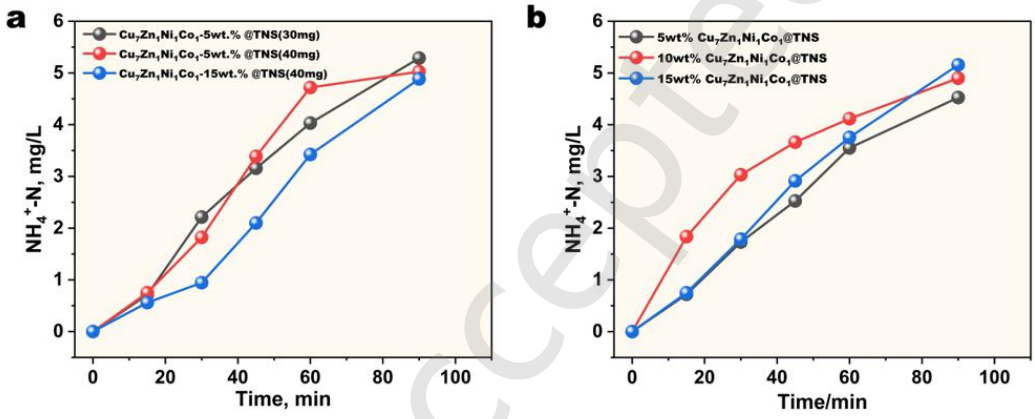

Figure S9. a) Optimization of the photocatalyst content; b) Optimization of the loading ratios of different metals with Cu as the primary element.

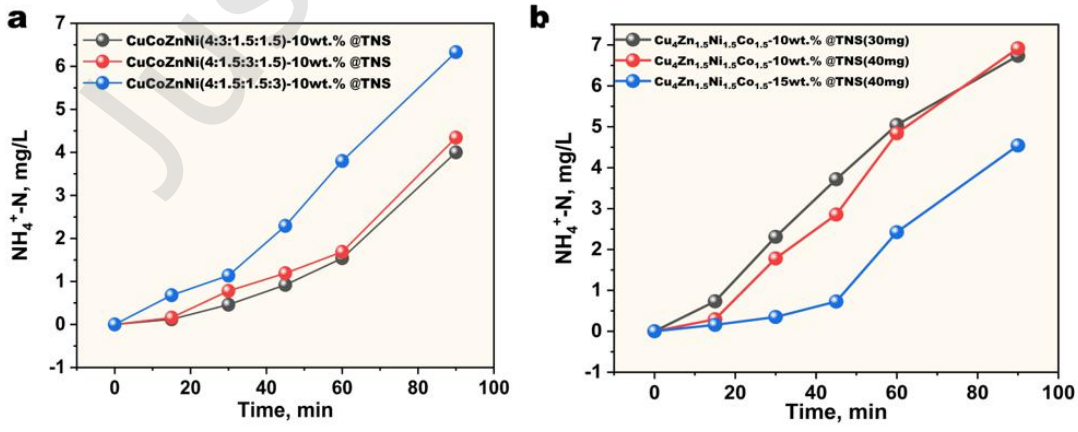

Figure S10. a) Photocatalytic efficiency with Cu as the primary element upon the addition of a second synergistic metal; b) Effects of co-metal loading ratios and overall catalyst content on photocatalytic efficiency with Cu as the primary element.

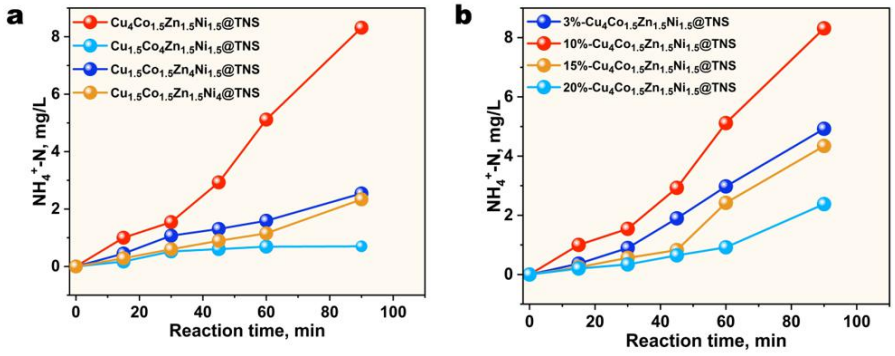

Figure S11. a) compares the photocatalytic performance of TiO_2-supported quaternary metal (Cu, Co, Ni, Zn) catalysts with each metal serving as the primary element, whereas (b) demonstrates that the optimal performance is achieved at a specific molar ratio (Cu: Co: Ni: Zn= 4:1.5:1.5:1.5) and a total metal loading of 10%.

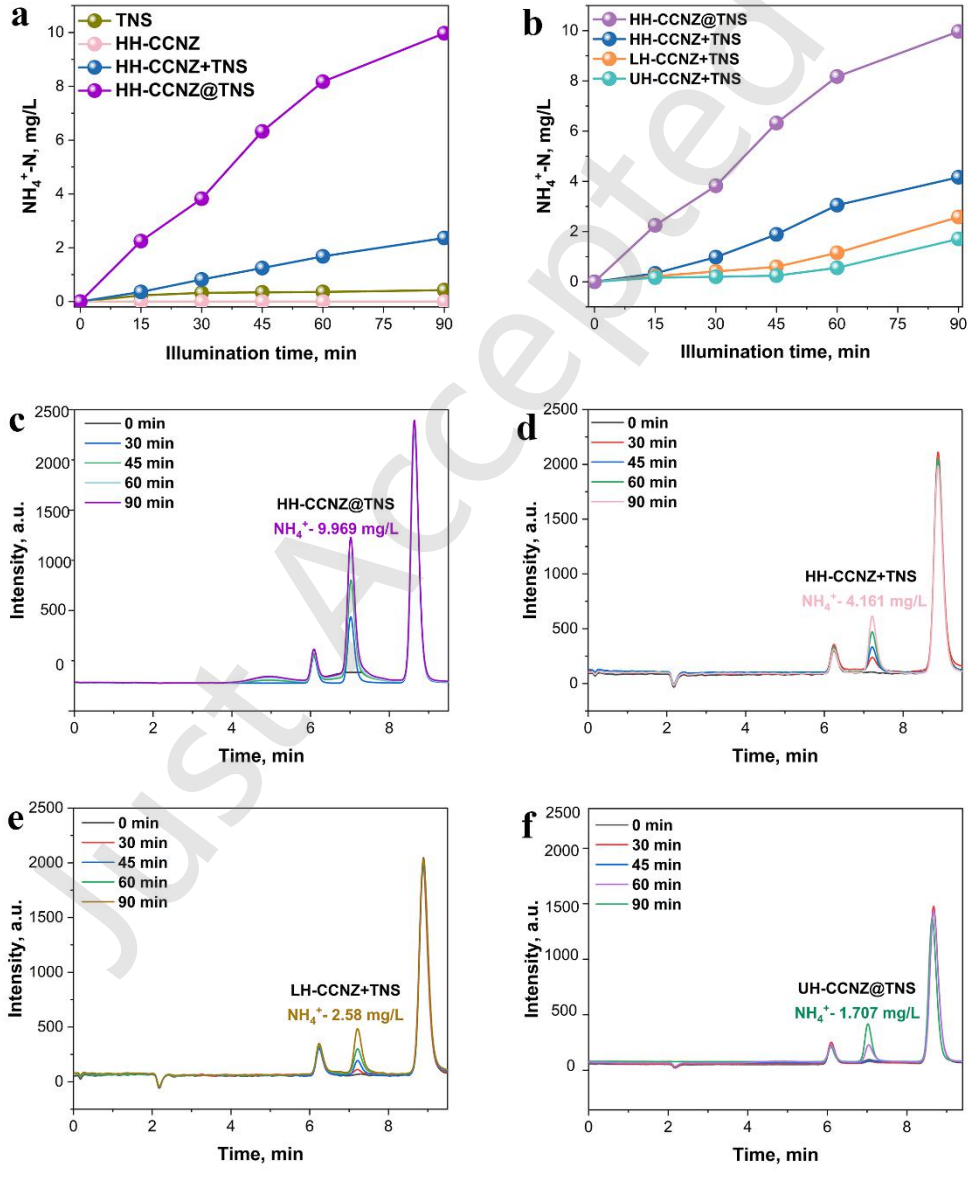

Figure S12. HH-CCNZ@TNS exhibits significantly higher photocatalytic activity in the reduction of nitrite to ammonia than the control group; at 90 minutes, the NH_4^+-N concentration reaches 10 mg/L, demonstrating that the interfacial coupling between HH-CCNZ and TNS significantly enhances carrier separation efficiency and reaction performance. Specifically, three control samples were prepared and evaluated under identical photocatalytic nitrite reduction conditions: LH-CCNZ+TNS, HH-CCNZ+TNS and UH-CCNZ+TNS.

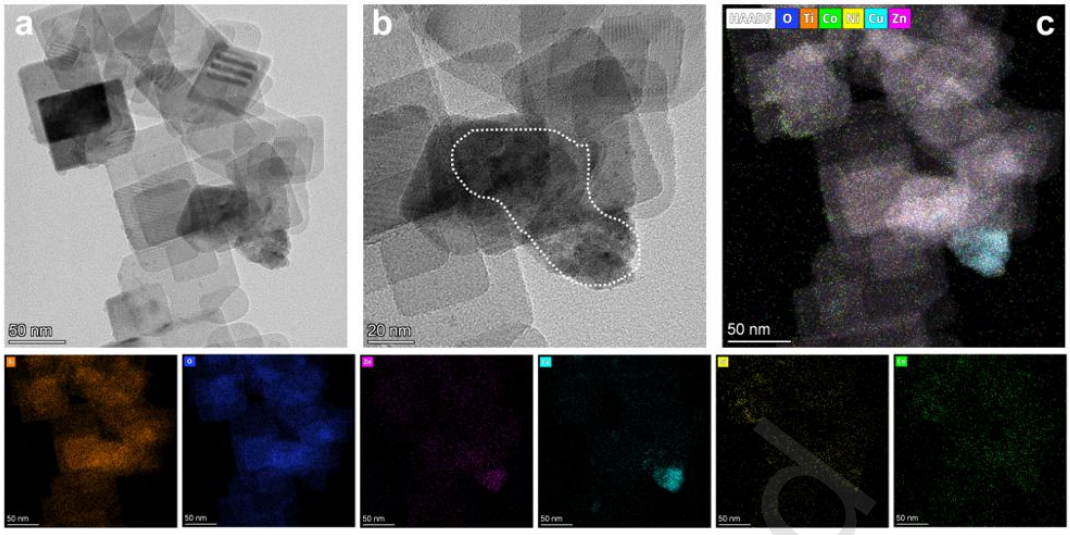

Figure S13. (a-c) TEM image and mapping spectra of the LH-CCNZ@TNS material after light irradiation.

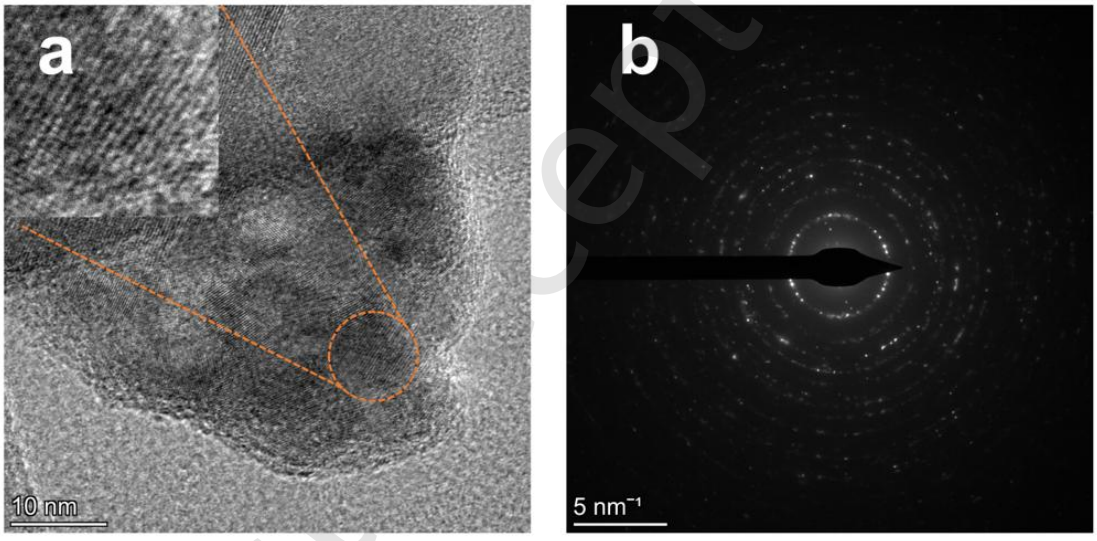

Figure S14. (a) demonstrates that the HRTEM image of the LH-CCNZ@TNS material after the light irradiation reaction reveals that the loaded medium-entropy alloy region has transformed from the previous amorphous phase to a crystalline phase. (b) shows the selected-area electron diffraction after the light irradiation reaction. After the photochemical reaction of the LH-CCNZ@TNS material, the alloy region undergoes crystallization.

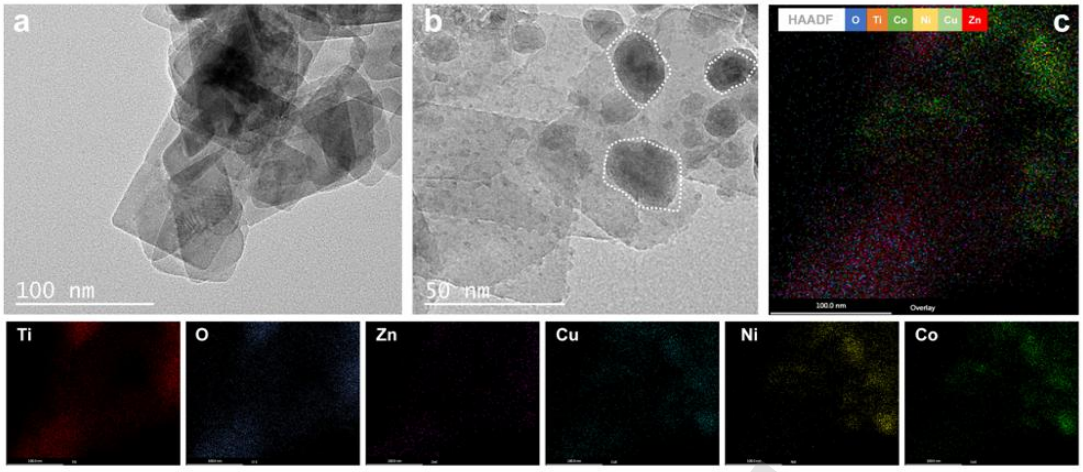

Figure S15. (a-c) TEM image and mapping spectra of the HH-CCNZ@TNS material after light irradiation.

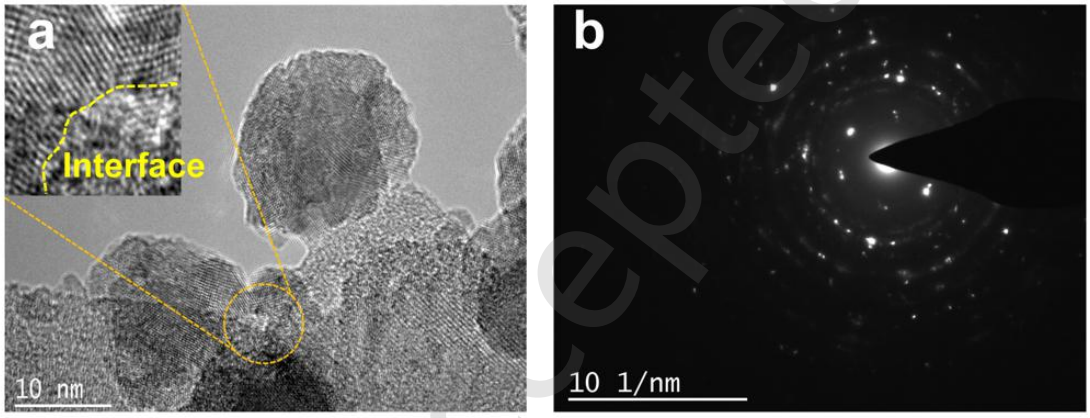

Figure S16. (a) indicates that the HRTEM image of the HH-CCNZ@TNS material after the light irradiation reaction shows that the loaded medium-entropy alloy region still retains its original crystalline/amorphous interface. (b) Electron diffraction pattern of the selected region of HH-CCNZ@TNS after exposure to light irradiation.

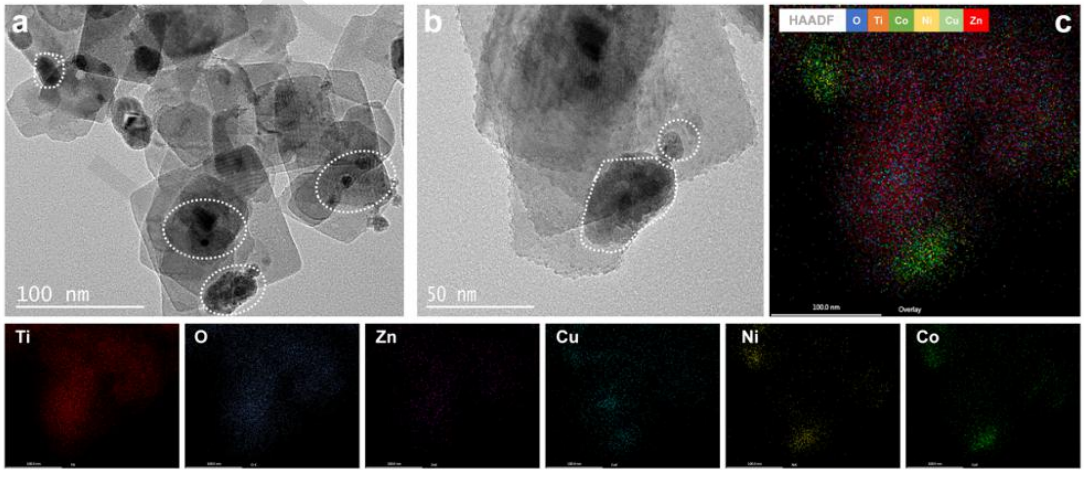

Figure S17. (a-c) TEM image and mapping spectra of the UH-CCNZ@TNS material after light irradiation.

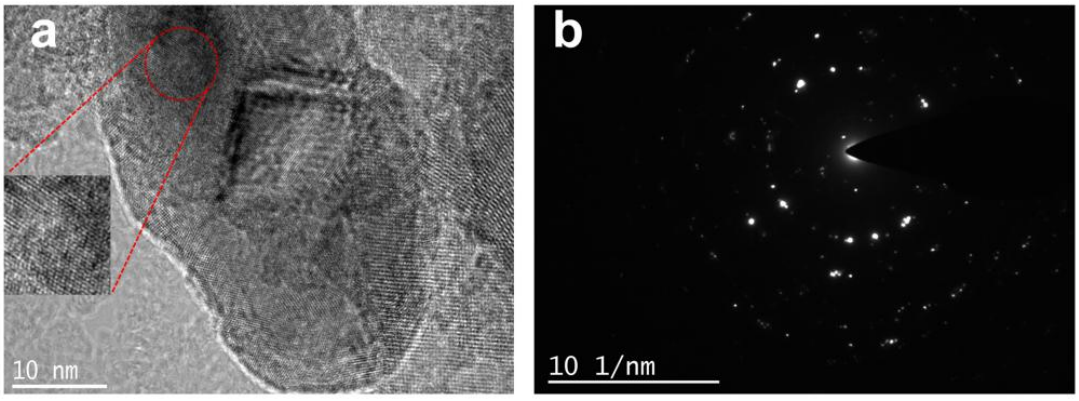

Figure S18. Figure a shows that the HRTEM image of the UH-CCNZ@TNS material after the light-induced reveals that the loaded medium-entropy alloy region still maintains its original crystalline state. Figure b shows the selected area electron diffraction pattern of UH-CCNZ@TNS after photoinduced reaction.

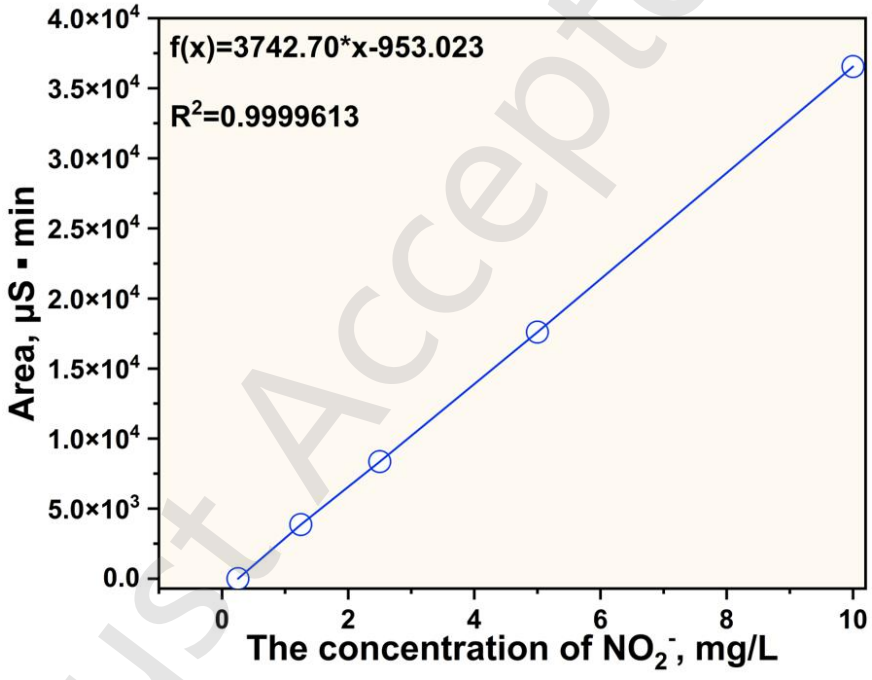

Figure S19. NO_2^- Nitrite Ion Standard Curve, calibration curve for nitrite nitrogen determination. The linear regression equation is f(x)= 3742.70x – 953.023, with a correlation coefficient (R^2) of 0.9999613.

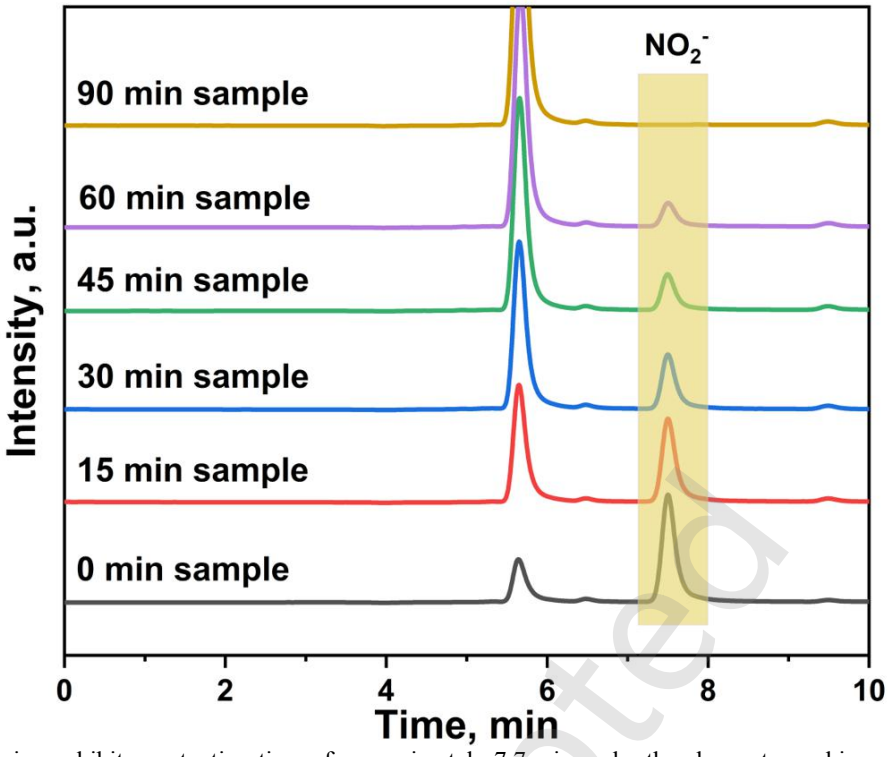

Figure S20. The nitrite ion exhibits a retention time of approximately 7.7 min under the chromatographic conditions using an IonPac AS11-HC column. The Figure above shows the continuous decrease in nitrite concentration during the photocatalytic nitrite reduction reaction catalyzed by the synthesized HH-CCNZ@TNS material.

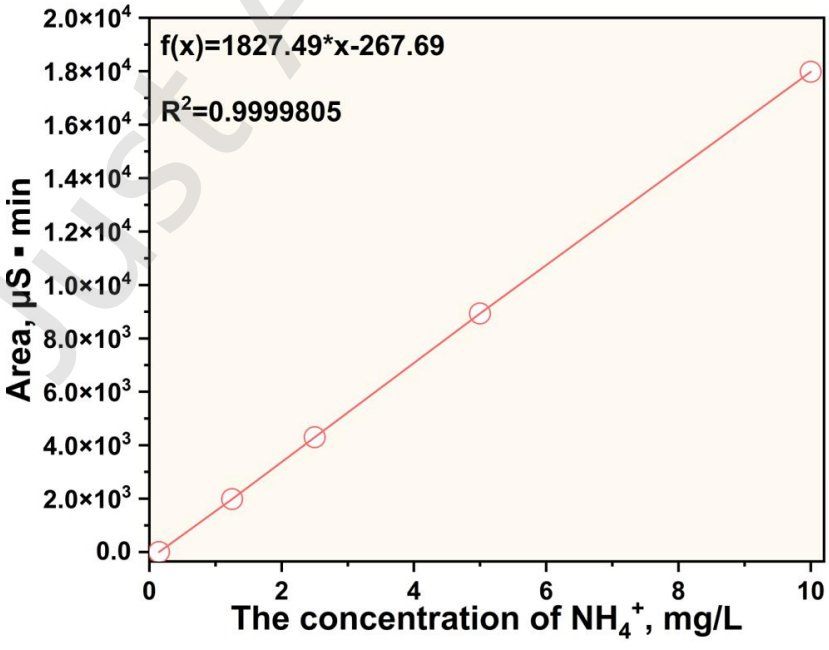

Figure S21. Ammonium Ion Standard Curve, standard curve for the quantification of ammonium ions (NH_4^+). The curve shows the linear relationship between the analytical signal (e.g., absorbance) and the NH_4^+ concentration. The linear regression equation is f(x) = 1827.49x – 267.69, with a correlation coefficient (R^2) of 0.9999805.

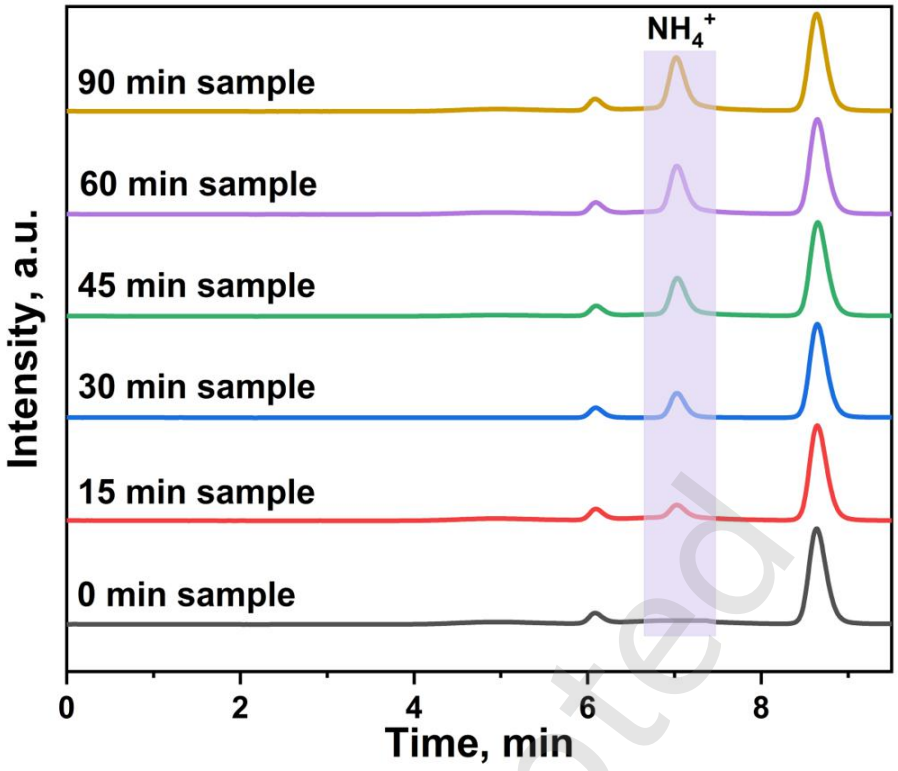

Figure S22. As shown in the Figure above, the photocatalytic nitrite-to-ammonia conversion catalyzed by HH-CCNZ@TNS exhibits continuously enhancing ammonia selectivity and conversion rate over time, as quantified by the peak areas in ion chromatography.

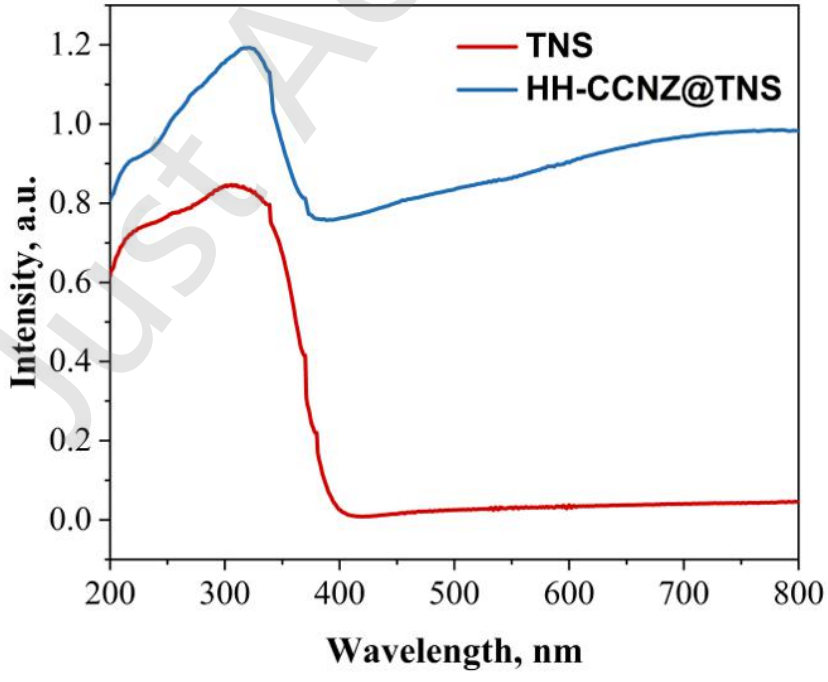

Figure S23. UV-Vis diffuse reflectance spectra: comparison of TNS and HH-CCNZ@TNS, showing extended light absorption range for HH-CCNZ@TNS.

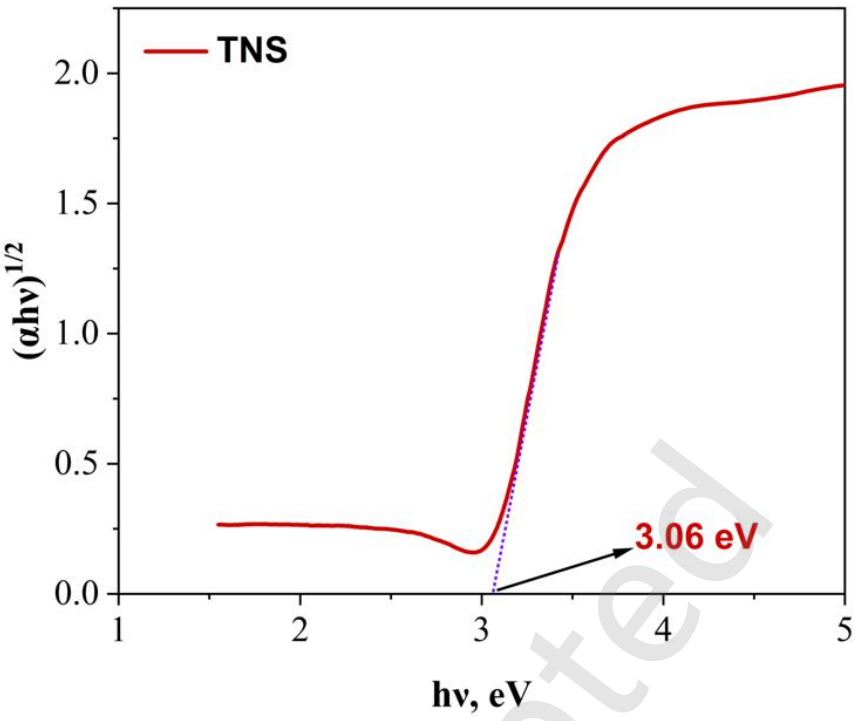

Figure S24. The Figure shows the $(\alpha h\nu)^{1/2}$–hν bandgap fitting curves for TNS and HH-CCNZ@TNS. The results indicate that the bandgap of TNS is 3.06 eV, suggesting that modification with the medium-entropy alloy has effectively reduced the bandgap width of the TiO_2-based material.

Table 1. Summary of various photocatalysts for the reduction of nitrous acid to NH_3

Photocatalyst	source of N	pH	Reducing agents	Detection method	Conversion (%)	NH_4^+ Selectivity (%)	NH_4^+ production rate (μ mol $g_{cat}^{-1}h^{-1}$)	long-term stability	ref
M/TiO_2	NO_2^-/ NO_3^-	5-6	N/A	indophenol-blue	N/A	N/A	2.4	N/A	[6]
ZnS	NO_2^-/ NO_3^-	7	sulphite	indophenol	N/A	N/A	25	N/A	[7]
Ni-ZnS	NO_2^-/ NO_3^-	N/A	methanol	indophenol	N/A	N/A	6.5	N/A	[8]
TiO_2	NO_2^-/ NO_3^-	N/A	N/A	indophenol	N/A	N/A	67	N/A	[9]
CdS	NO_2^-	<7	sulphite	indophenol	N/A	N/A	33	N/A	[10]
$Nf(TiO_2$-$Au)_{nps}$/ $[Ni(teta)]^{2+}$	NO_2^-	N/A	oxalic acid	Nessler's reagent	N/A	N/A	127	N/A	[11]
CuCoNiZn @TNS	NO_2^-	N/A	potassium nitrite	UV-vis	N/A	N/A	884	N/A	This work

References

[1] Zhang, H.; Sun, P.; Fei, X.; Wu, X.; Huang, Z. Unusual facet and co-catalyst effects in TiO_2-based photocatalytic coupling of methane. *Nat. Commun.* **2024**, *15*, 4453**.**

[2] Chen, X.; Zhai, S.; Tan, Y.; Su, L.; Zhai, D. Enhanced nitrite electroreduction to ammonia via interfacial dual-site adsorption. *J. Energy Chem.* **2024**, *96*, 328–335.

[3] Wang, L.; Yan, Y.; Han, X.; Jianguo Yu. Interfacial water engineering via amorphous-crystalline hybrids for neutral nitrate electroreduction to ammonia. *Appl. Catal. B.* **2025**, *25*, 125813.

[4] Carrasco, E.; Campos-Vallette, A.; P. Leyton, F.; Diaz; Clavijo, R. Study of the interaction of pollutant nitro polycyclic aromatic hydrocarbons with different metallic surfaces by surface-enhanced vibrational spectroscopy (SERS and SEIR). *J Phys Chem A.* **2003**, *108,* 9611–9619.

[5] Zhao, J.; Huang, K.; Liu, C.; Wu, X.; Ning, Y. Electro‐induced crystallization over amorphous indium hydroxide gels toward ampere‐level current density formate electrosynthesis. *Adv. Funct. Materials.* **2024**, *34*, 2316167.

[6] KT, R.; Viswanathan, B. Photocatalytic reduction of nitrite and nitrate ions to ammonia on M/TiO_2 catalysts. *J. Photochem. Photobiol. A.* **1997**, *108*, 73–78.

[7] Ranjit, K.; Krishnamoorthy, R.; Viswanathan, B. Photocatalytic reduction of nitrite and nitrate on ZnS. *J. Photochem. Photobiol. A.* **1994**, *81*, 55–58.

[8] Hamanoi, O.; Kudo, A. Reduction of nitrate andnitrite ions over Ni-ZnS photocatalyst under visible light irradiation in the presence of a sacrificial reagent. *Chem. Lett.* **2002**, *31*, 838–839.

[9] Ranjit, K.; Viswanathan, B.; Varadarajan, T. Photocatalytic reduction of nitrite and nitrate ions over TiO_2 semiconductors. *J. Mater. Sci. Lett.* **1996**, *15*, 874-877.

[10] Ranjit, K.; Krishnamoorthy, R.; Varadarajan, T.; Viswanathan, B. Photocatalytic reduction of nitrite on CdS. *J. Photochem. Photobiol. A.* **1995**, *86*, 185–189.

[11] Pandikumar, A.; Manonmani, S.; Ramaraj, R. TiO_2-Au nanocomposite materials embedded in polymer matrices and their application in the photocatalytic reduction of nitrite to ammonia. *Catal. SciNO.Technol.* **2012**, *2*, 345–353.